AFRL-VS-HA-TR-2007-1030

# Continent-wide Maps of Lg Coda Q Variation and Rayleigh-wave Attenuation Variation for Eurasia

**Brian J. Mitchell**
**Lianli Cong**

**Saint Louis University**
**221 N. Grand Blvd.**
**St. Louis, Missouri 63103**

**Final Report**

**30 January 2007**

**APPROVED FOR PUBLIC RELEASE; DISTRIBUTION UNLIMITED.**

**AIR FORCE RESEARCH LABORATORY**
**AIR FORCE MATERIEL COMMAND**
**Space Vehicles Directorate**
**29 Randolph Rd.**
**Hanscom AFB, MA 01731-3010**

## NOTICES



AFRL-VS-HA-TR-2007-1030 HAS BEEN REVIEWED AND IS APPROVED FOR PUBLICATION IN ACCORDANCE WITH ASSIGNED DISTRIBUTION STATEMENT.

| | |
|---|---|
| //Signature// | //Signature// |
| ROBERT J. RAISTRICK<br>Contract Manager | ROBERT BELAND, Chief<br>Battlespace Surveillance Innovation Center |

# 0REPORT DOCUMENTATION PAGE

*Form Approved*
*OMB No. 0704-0188*



**1. REPORT DATE** *(DD-MM-YYYY)*
30 January 2007

**2. REPORT TYPE**
Final Report

**3. DATES COVERED** *(From - To)*
7 Jun 2004 to 6 Jun 2006

**4. TITLE AND SUBTITLE**
Continent-wide Maps of Lg Coda Q Variation and Rayleigh-wave Attenuation Variation for Eurasia

**5a. CONTRACT NUMBER**
FA8718-04-C-0021

**5b. GRANT NUMBER**

**5c. PROGRAM ELEMENT NUMBER**
62601F

**6. AUTHOR(S)**
Brian J. Mitchell and Lianli Cong

**5d. PROJECT NUMBER**
1010

**5e. TASK NUMBER**
SM

**5f. WORK UNIT NUMBER**
A1

**7. PERFORMING ORGANIZATION NAME(S) AND ADDRESS(ES)**

Saint Louis University
221 N. Grand Blvd.
St. Louis, Missouri 63103

**8. PERFORMING ORGANIZATION REPORT NUMBER**

**9. SPONSORING / MONITORING AGENCY NAME(S) AND ADDRESS(ES)**
Air Force Research Laboratory
29 Randolph Road
Hanscom AFB, MA 01731-3010

**10. SPONSOR/MONITOR'S ACRONYM(S)**
AFRL/VSBYE

**11. SPONSOR/MONITOR'S REPORT NUMBER(S)**
AFRL-VS-HA-TR-2007-1030

**12. DISTRIBUTION / AVAILABILITY STATEMENT**
Approved for Public Release; Distribution Unlimited.

**13. SUPPLEMENTARY NOTES**

**14. ABSTRACT**

We present new maps of Lg coda Q and its frequency dependence at 1 Hz ($Q_o$ and η, respectively) as well as Rayleigh-wave attenuation coefficients at 5, 10, 20 and 50 s across virtually all of Eurasia. $Q_o$ is relatively high, 700 or more, in most cratonic regons but is surprisingly low in the Arabian craton (300-450), the Siberian trap portion of the Siberian Platform (~450) and the Deccan trap portion of the Indian Platform(450-650). It is generally low throughout the Tethysides orogenic belt but there too it displays substantial regional variations (150-400). All major $Q_o$ anomalies, and several minor ones, appear to be related to the tectonic history of the Eurasian crust. The four regions with lowest values approximately coincide with four of Eurasia's most active concentrations of earthquake activity. Comparison of the new $Q_o$ map with continent-wide maps of long-period Rayleigh-wave phase velocities, temperatures, subducted lithosphere and crustal strain lead us to infer that fluids, originating by hydrothermal release from subducting lithosphere or other upper mantle heat sources largely produce the observed variations of $Q_o$ across Eurasia. We estimated Rayleigh-wave attenuation coefficients across Eurasia, at periods of 5, 10, 20 and 50 s, using mapped values for $Q_o$, η and an empirically derived multiplicative factor for η. 5 and 10 s attenuation values clearly show several attenuation maxima that are with thick accumulations of sediment, whereas the longer period attenuation, in most cases, mirror the $Q_o$ map. Differences, however, occur in some regions because because of high or low η values.

**15. SUBJECT TERMS**
Lg, Rayleigh waves, Q, Attenuation, Eruasia

| 16. SECURITY CLASSIFICATION OF: | | | 17. LIMITATION OF ABSTRACT | 18. NUMBER OF PAGES | 19a. NAME OF RESPONSIBLE PERSON |
|---|---|---|---|---|---|
| | | | | | Robert J. Raistrick |
| **a. REPORT** UNC | **b. ABSTRACT** UNC | **c. THIS PAGE** UNC | SAR | 46 | **19b. TELEPHONE NUMBER** *(include area code)* 781-377-3726 |

**Standard Form 298 (Rev. 8-98)**
**Prescribed by ANSI Std. 239.18**

# Table of Contents

## Figures

# 1 INTRODUCTION

Eurasia is Earth's youngest continent and contains its most spectacular tectonic features. It provides an excellent laboratory in which to study possible relationships between $Q$ variations and regional tectonics. For that purpose we start by studying $Lg$ coda $Q$ ($Q_{Lg}^C$), a phase that is typically described by $Q_o f^\eta$ where $Q_o$ and $\eta$ represent, respectively, the $Q$ value and frequency-dependence parameter of $Lg$ coda $Q$ at 1 Hz. Knowledge of $Q_o$ and $\eta$ variation across Eurasia allows us to relate those quantities to other geophysical properties of the crust and upper mantle across Eurasia and also to develop maps of fundamental-mode Rayleigh-wave attenuation coefficients for Eurasia.

Specifically, this study addresses three different, but related, issues. First, we present new maps of $Q_o$ and $\eta$ that cover virtually all of conterminous Eurasia. The new maps should provide a starting point for more detailed studies in smaller regions and for studies of $Q$ variation at other frequencies.

Second, we compare the distribution of $Q_o$ values with earthquake distribution, past tectonic activity and areal distributions of several geophysical properties. Those comparisons lead us to present an extended version of our earlier model for explaining seismic $Q$ variation in terms of the emplacement and subsequent dissipation of fluids in the continental crust.

Third, we utilize the maps of $Q_o$ and $\eta$ to develop the first continent-wide maps of Rayleigh-wave attenuation for Eurasia at periods of 5, 10, 20 and 50 s. To our knowledge, these are the first maps of surface-wave attenuation to be developed for any entire continent, at least for short to intermediate period ranges.

# 2 TECTONIC EVOLUTION OF EURASIA: AN OVERVIEW

This section presents a broad overview of the known tectonic history of Eurasia, emphasizing those aspects that appear to correlate closely with large-scale $Q$ variations within the continent. Later sections will add further tectonic and geological details for specific regions where the relation of $Q$ to tectonics warrants further discussion.

Several broad-scale studies of Eurasian tectonics provide information that is useful for interpreting observed $Q$ variation across that continent. *Zonenshain et al.* (1990) discuss the evolution of the entire Eurasian continent, but emphasize the more stable northern and central regions. *Sengör* (1984, 1987) presents detailed discussions of the Cimmeride system and the Tethysides system (or Alpine-Himalayan collision zone). *Sengör and Natal'in* (1996) provide a detailed exposition of the paleotectonics of Asia and *Ziegler* (2005) provides up to date information on the Permian to Recent tectonic evolution of Europe. We have drawn upon these sources in our limited discussions of Eurasian tectonics in this and following sections.

The simplified tectonic map in Figure 1 includes major tectonic features of Eurasia that appear to be related to regional variations in $Q_{Lg}^C$. Other mapped tectonic features, however, are conspicuous by their lack of association with a $Q$ anomaly. We will discuss both types of feature in more detail in later sections. *Zonenshain et al.* (1990) indicate that Eurasia has formed by the coalescence of numerous crustal blocks beginning in the early Paleozoic and continuing to the present time. The East European and Siberian Platforms in northern Eurasia

had previously formed from the coalescence of smaller continental blocks, the process reaching completion, respectively, in about 1700 Ma and 1600 Ma for the two platforms. Extensive intraplate volcanism occurred in the Siberian, but not the East European Platform from Precambrian to Cretaceous time, the most extensive being the Siberian traps that were extruded in an extensional environment between 255 and 245 Ma.

The Altaids, a collage of late Protoerozoic to early Mesozoic orogenic belts, separates the East European and Siberian Platforms and its eastward-trending arm extends around the southern part of the Siberian Platform nearly reaching the Sea of Okhotsk. Much of that collage was formed from giant Paleozoic subduction-accretion complexes and from the development of subduction-related sedimentation and magmatism (*Sengör et al.*, 1993). Those processes are thought to have added about 5.3 million $km^2$ of material to Asia, significantly contributing to its growth during the Paleozoic era.

The East European craton, along with the rest of Laurentia, collided with the Altaid complex and the Siberian craton beginning at about 310 Ma. This collison, along with the accretion of many smaller plates produced a single Laurasia at about 280 Ma. The Altaids at that time prevented further convergence of the Siberian and East European cratons but was reduced in size when orogeny along its western margin producing the Ural Mountains. At the same time the Paleo-Tethys plate converged with Laurasia from the south along an east-west striking zone that stretched for about 6000 km. As the Paleo-Tethys plate was being consumed beneath Eurasia, the newly formed Neo-Tethys plate, which had been separated from the Paleo-Tethys by the Cimmerian continent, widened over much of its length.

Collision of the North China block with Eurasia and closure of the Paleo-Tethys Sea caused an extensive reorganization of the various plates at about 220 Ma. Compression within Eurasia ceased completely while parts of western Siberia and the Barents Sea basin entered an extensional stage.

Pangea, the supercontinent resulting from previous plate interactions, began to break up about 160 Ma as the Africa-Arabia plate began to converge with Eurasia. Both processes ended by about i 130 Ma. Eurasia separated from North America at about 80 Ma while exotic terrains from the Pacific continued to accrete to its eastern margin.

During the Cenozoic era Eurasia began to converge with India in the south while continuing to converge with Africa-Arabia in the southwest. Both processes continue to contribute to narrowing of the Tethys ocean.

Ensuing sections will show that the relative youth of Eurasia's complex evolutionary history explains why average $Q$ values there are generally lower than are average values in the crusts of Africa, South America and much of the stable portions of North America. They will also show that processes associated with current plate collisions along the southern and eastern margins of Eurasia largely explain the low $Q_o$ values in those regions.

## 3 DATA AND DETERMINATION OF $Q_o$ AND $\eta$

A map of the earthquakes and recording stations used in this study appears in Figure 2. 666 earthquakes and 21 stations on the map are new and provide new recordings of $Lg$ coda for 943 earthquake-station pairs. The new determinations, when combined with 440 values from

*Mitchell et al.* (1997) yield a total of 1383 determinations for both $Q_o$ and $\eta$. The new data provide new coverage for northeastern Siberia, where the largest gap previously existed, as well as for Spain and southeastern Asia. In addition, we achieved much improved coverage in eastern China, Siberia, India and the Himalaya.

*Lg* coda has several characteristics that make it suitable for tomographic $Q$ mapping. First, since it is a scattered wave, it can continue to oscillate for several hundred seconds following the onset of the direct *Lg* phase, allowing compution of spectral amplitude ratios from several pairs of windows along the time series and to stack those ratios to obtain reliable estimates of $Q_o$ and $\eta$. Second, its energy travels predominantly in the crust, thus providing estimated average values of crustal $Q$ through a known depth interval. Third, it is a large and easily recognizable phase for which useable recordings can be generated by even relatively small earthquakes; thus data, in most regions is plentiful.

We determine $Q_o$ and $\eta$ using the Stacked Spectral Ratio (*SSR*) method (*Xie and Nuttli*, 1988). This single-trace method takes ratios of spectral amplitudes for selected pairs of windows along a trace of 300 or more seconds duration; this process cancels any effects of source complexity or instrumental effects. A detailed description of the *SSR* method appears in *Xie and Nuttli* (1988) and more briefly in *Mitchell et al.* (1997).

Three examples of seismograms that include *Lg* and its coda for Eurasian paths appear in Figure 3. Measured values of $Q_o$ decrease from top to bottom in the figure. The top trace is for a relatively high-$Q$ (701) path to station HYB in India, the bottom trace is for a low-$Q$ (208) path to station LSA in Tibet and the middle trace is from a path to station BJT in northern China where $Q$ (359) is intermediate between the other two. The traces show a progression of decreasing predominant coda frequencies and amplitudes with decreasing $Q$ value.

*SSR* plots appear to the right of each trace. Portions of all three traces form an approximate straight line on a log-log plot that can be fit by least squares. The value of $Q^{-1}$ and slope of the best- fitting line at 1 Hz yields, respectively, values for $Q_o$ and $\eta$. Inversions of sets of those values over a broad region yield tomographic maps of those quantities.

It is important to emphasize that, because they are derived using observed scattered energy of *Lg* coda that is areally represented by ellipses, our maps do not include effects of *Lg* blockage reported in regions such the North Sea Graben (*Gregersen*, 1984; *Kennett et al.*, 1985), the Barents Shelf (*Baumgardt*, 2001) and some portions of the Middle East (*Kadinsky-Cade et al.*, 1981; *Sandvol et al.*, 2001). We have no data from the blocked paths, but are likely to have data for other paths, such as those sub-parallel to the blocking feature or for which the source or recording station, represented by one focus of the scattering ellipse, lies near the blocking feature. In both cases portions of the scattering ellipses that appear in Figure 4 will overlap the blocking feature, but that feature will not substantially contribute to the values we obtain for $Q_o$ and $\eta$.

# 4 MAPPING $Q_o$ and $\eta$ - METHODOLOGY

A detailed discussion of the inversion method for mapping $Q_o$ and $\eta$ appears in *Xie and Mitchell* (1990a) and more briefly in *Mitchell et al.* (1997). The method assumes that the area occupied by the scattered energy of recorded *Lg* coda can be approximated by an ellipse with the source

at one focus and the recording station at the other, as was shown theoretically by *Malin* (1978) to be the case for single scattering.

The process utilizes a back-projection algorithm for producing tomographic images of $Q_o$ and $\eta$ over a broad region using a number ($N_d$) of $Q_o$ or $\eta$ values determined from observed ground motion. Figure 4 shows the ellipses corresponding to all event-station pairs used in Eurasia. The inversion process assumes that each ellipse approximates the spatial coverage of scattered energy comprising late $Lg$ coda. The areas of the ellipses vary with lag time of the $Lg$ coda components and will be larger for later times. The ellipses in the figure are plotted for maximum lag times used in the determination of $Q_o$ and $\eta$. It is best to have as much overlap of ellipses as possible to obtain redundancy that is beneficial in the inversion process.

We divided Eurasia into $N_c$ cells with dimensions $3^o$ by $3^o$, based upon theoretical resolution over which $Q_o$ will have constant value. Following *Xie and Mitchell* (1990a) we assume that the $Q_n$ value for each trace corresponds to the areal average of the cells covered by its ellipse. If the area over which the ellipse for the $n^{th}$ trace overlaps the $m^{th}$ cell is $s_{mn}$ then

$$\frac{1}{Q_n} = \frac{1}{S_n} \sum_{m=1}^{N_c} \frac{S_{mn}}{Q_m} + \epsilon \qquad n = 1, 2, \cdots, N_d \tag{1}$$

where

$$S_n = \sum_{j=1}^{N_c} S_{jn}, \tag{2}$$

and $\epsilon$ is the residual due to the errors in the measurement and modeling of $Lg$ coda. Back-projection, or the Algebraic Reconstruction Technique (*Gordon*, 1974) has been applied in several tomographic mappings of seismic velocity (e.g. *McMechan*, 1983; *Humphreys and Clayton*, 1988) and is convenient for our purposes.

We obtain a tomographic map of the frequency dependence of $Q_{Lg}^C$ at 1 Hz by using the $N_d$ values for $Q_o$ and $\eta$ obtained at that frequency to estimate $Q_{Lg}^C$ at another frequency which we take to be 3 Hz. The 3-Hz values become $Q_n$ in equation 1 and an inversion yields a map of $Lg$ coda $Q$ at that frequency. A map of the frequency dependence of $Lg$ coda $Q$ is then obtained using

$$\eta = \frac{1}{\ln 3} \ln \frac{Q(f)3Hz}{Q_o} \tag{3}$$

For the back-projection process it is convenient to use the "point spreading function" ($psf$) suggested by *Humphreys and Clayton* (1988) as a measure of resolution. It is obtained by constructing a model in which $Q^{-1}$ is unity in a cell of interest and zero in all other cells. Determination of average $Q_o$ values for all elliptical areas in Figure 4 for that model then yields a synthetic data set that can be inverted to see how $Q_o^{-1}$ varies around each selected cell. This inversion yields the $psf$ pertaining to the region of the selected and surrounding cells. The area and falloff with distance from the central cell provides an estimate of resolution.

The effect that random noise included in $Lg$ coda has on images of $Q_o$ and $\eta$ can be tested empirically using the sample standard error in $Q_n$ caused by randomness of the $SSR$s (*Xie and Nuttli*, 1988). If the standard error of $Q_n$ is denoted by $\delta Q_n$, $n = 1, 2, N_d$, and if we assume that $\delta Q_n$ gives a good measure of the absolute value of the real error preserved in the $Q_n$ measurements, we can construct a number of noise series whose $m_{th}$ member has an absolute

value equal to $\delta Q_n$ and a sign that is chosen randomly. The $n^{th}$ term of the noise series is added to $Q_n$ and the sums of the two series are then inverted to obtain a new $Q_m$ image from which the original one is subtracted to yield an error estimate of the $Q_n$ values. Since the sign of $\delta Q_n$ was determined using a random binary generator, it is important to repeat the process several times and obtain an average error estimate.

# 5 New $Q_o$ and $\eta$ Maps

Figures 5 and 6 show new continent-wide maps of $Q_o$ and $\eta$ for Eurasia. They differ from earlier continent-wide maps of that continent (*Mitchell et al.*, 1997) by providing much new and improved coverage as described earlier. The broad-scale features of the new $Q_o$ map are virtually the same as those of *Mitchell et al.* (1997) for regions where there is common coverage. These include low values (150 - 400) throughout, and extending slightly north of, the Tethysides orogenic belt, the active region resulting from the collision of the Afro/Arabian and Indian plates with Europe and Asia, and significantly higher values (as high as 950 or more) throughout most of the stable northern portions of Eurasia as well as the Indian platform. The new map supports unexpected earlier results (*Mitchell et al.*, 1997) that indicate relatively low values in central Siberia, the Arabian Peninsula, the British Isles and France.

Figure 6 presents the distribution of $\eta$, the frequency dependence of $Q_{Lg}^C$ at 1 Hz. Since its determination requires differencing $Q_o$ values obtained at two frequencies, the uncertainties in mapped values of $\eta$ are higher than for $Q_o$. $\eta$ values are generally higher (0.7 - 0.9) in regions where $Q_o$ is high (e.g. northern Eurasia and southern India) and are low (e.g. most of southern and eastern Eurasia) where $Q_o$ is low. The opposite relation, however, occurs in Spain and the British Isles, where $Q_o$ is low and $\eta$ is high. These results may all be correct but it is possible that $\eta$ determinations for Spain and the British Isles are biased by systematic errors that occur in the differencing process for determining $\eta$. Systematic errors in those regions are more likely because of the possibility that the continent-ocean transition may bias measured $Q_o$ values (*Xie and Mitchell*, 1990b).

Figures 7 and 8 map standard errors for $Q_o$ and $\eta$. $Q_o$ standard errors lie between 0 and 50 throughout most of Eurasia but are between 50 and 100 in a few places and quite high (200-250) in a region to the southwest of Lake Baikal and in the northwestern corner of the map. The high standard errors near Lake Baikal coincide with a region that stood out as being laterally anomalous in a recent study of shear-wave $Q$ variation (*Jemberie and Mitchell*, 2004). The pattern of $\eta$ standard error variation is generally similar to that of $Q_o$, being between 0.0 and 0.1 throughout most of the continent and between 0.1 and 0.2 in most other places. It is again higher to the southwest of Lake Baikal and in the northwestern-most corner of the map. $psf$ patterns for six selected cells appear in Figure 9. They indicate that our ability to resolve features across Eurasia is about the same everywhere.

Assigning numbers to this resolvability is somewhat subjective, depending upon the fraction of the maximum value we choose to indicate resolvability. It appears, however, that we can resolve features between about 600 and 900 km in length in most regions. This marks a significant improvement over resolution in *Mitchell et al.* (1997) where the $psf$'s in poorly sampled regions sometimes implied a resolution length of 1200 km or more.

# 6 RELATION OF SPATIAL $Q_o$ VARIATIONS TO UPPER MANTLE PROPERTIES AND PROCESSES: SEISMIC VELOCITY, TEMPERATURE AND SUBDUCTED LITHOSPHERE

One of the goals of this study is to explain the large-scale variations of $Q_o$ observed across Eurasia. Toward that goal we have compiled continent-wide maps showing patterns of 100-s Rayleigh-wave velocity variation, temperature and plate subduction in the mantle and of seismicity at crustal depth. That information has been supplemented with maps of 20-s Rayleigh-wave group velocities in the Arabian Peninsula and further information from the literature. Patterns in all of the maps show clear similarities that indicate a prominent role of mantle processes in producing the main features of our map of $Q_o$ variation (Figure 5). With the exception of seismicity, none of these data sets were available, at least on continental scales, at the time of the *Mitchell et al.* (1997) study.

Past studies, as discussed earlier, have shown that several factors may contribute to reductions in $Q_o$; these include thick accumulations of young sediments (*Mitchell and Hwang*, 1987) and the presence of a velocity gradient rather than a sharp interface at the crust/mantle boundary (*Bowman and Kennett*, 1991; *Mitchell and Cong*, 1998). In addition, decreasing depth of the Moho in the direction of $Lg$ travel or undulations of the Moho surface can be expected to decrease measured $Q_o$. Degradation in $Q_o$ determinations due to these factors are likely to cause formal determinations of correlation cofficients to be low (e.g. *Zhang and Lay*, 1994; *Artemieva et al.*, 2004).

In this section we discuss continent-wide compilations of long-period surface-wave phase velocities, temperatures and estimates of volumes of subducted lithosphere over the past 110 My. Each of these compilations is described in the paragraphs below along with a discussion of possible conclusions to be drawn when comparing them to the $Q_o$ and $\eta$ maps in Figures 5 and 6.

## 6.1 100-s Rayleigh-wave phase velocities

Figure 10 presents a map of Rayleigh-wave phase-velocity ($C_R$) variations relative to those predicted by the PREM model (*Dziewonski and Anderson*, 1981) across all of conterminous Eurasia at a period of 100 s. One-dimensional sensitivity kernels in Figure 11 indicate that peak sensitivities (partial derivatives of phase velocity wrt shear velocity) occur primarily through the depth range 100-200 km with little or no sensitivity to shear-velocity at crustal depths (70 km or less).

A comparison of of mapped 100-s Rayleigh-wave phase velocities in Figure 10 with the mapped $Q_o$ variations in Figure 5 shows striking similarities between $C_R$ and $Q_o$ patterns even though $C_R$ values are controlled by elastic properties of the upper mantle and $Q_o$ values by anelastic properties of the crust. The broad band of low crustal $Q$ values in the Tethysides belt of southern Eurasia mirrors well the low seismic velocities that must lie at upper mantle depths. Even in northern India and its northern periphery, the somewhat higher velocities (light blue) in the Tethysides belt correspond to a 1500-2000 km wide portion of the belt where $Q_o$ is higher than in regions to the east or west. Both the low mantle velocities and the low crustal $Q$ values that characterize the Tethysides belt extend farther north than the northern boundary of the

Tethysides as mapped by (*Sengör*, 1987). For most portions of the belt, especially in Europe and westernmost Asia, low crustal $Q$ values extend somewhat further north than do the low mantle velocities.

Another interesting similarity in mapped of patterns between crustal $Q_o$ and mantle velocities lies in northern Siberia. Its northernmost point lies near the Arctic coast at about $75^o$ E longitude and it trends in a south-southeast direction from there. This low-$Q$, low-velocity anomaly coincides with the Siberian traps mapped by *Reichow et al.* (2002) on the basis of new $^{40}$Ar/$^{39}$Ar data. That $Q_o$ anomaly appeared in *Mitchell et al.* (1997) but earlier mappings of the Siberian Traps, available at that time, did not correlate well with that anomaly.

$Q_o$ increases with increasing 100-s $C_R$ almost everywhere in Eurasia, but an exception occurs in the Arabian Peninsula where $Q_o$ decreases from west to east from the shield portion of the peninsula to the platform with increasingly thick sediments proceeding eastward. We discuss that apparently anomalous result in the following section in connection with our comparison of $Q_o$ variation with 20-s Rayleigh-wave group-velocity variation across the Arabian Peninsula. The similar patterns for crustal and upper mantle properties shown in Figures 5 and 10 suggest that variations in our maps of $Q_o$ have their origin in upper mantle processes. This inference is supported by results of the following section that discusses upper mantle temperature variations across Eurasia. The discusson section presents a model for explaining these variation that is consistent with available geophysical information.

### 6.2 Upper mantle temperatures

*Artemieva and Mooney* (2001) presented global maps of heat flow and estimated temperatures at various depths with emphasis on cratonic regions and *Artemieva et al.* (2004) compared global maps of thermal structure of continental mantle with global $1/Q_\mu$ and shear-wave velocities at upper mantle depths. They found that, at a depth of 100 km where velocity and $1/Q_\mu$ resolutions are highest, temperature variations can explain $1/Q_\mu$ and shear-wave velocities in much of the world's continental regions. Consequently, we have plotted the Eurasian portion of the *Artemieva and Mooney* (2001) temperature map at a depth of 100 km (Figure 12) for comparison with our map of $Q_o$ variation.

For our comparison of $Q_o$ with temperature there are several uncertainties in the temperature determinations that must be kept in mind. First, there are large gaps in coverage especially in active regions of southern Asia and eastern Europe, including Tibet, the Himalaya, the Caucasus and the Carpathians (I.M Artemieva, personal communication). In those regions mantle temperatures were estimated from data reported in the literature and under the assumption that the thermal thickness (i.e. where temperature is 1300C) is 80-90 km. In the Arabian peninsula, a region important in this study, all heat flow determinations are from a single study by *Gettings et al.* (1986) that was restricted to a relatively small region of southern Saudi Arabia. All measurements indicated that heat flow values were typical for stable continental regions. It is reasonable to assume that those heat flow values characterize the entire peninsula which, except for differing thicknesses of sediments, appears to have a relatively uniform structure and tectonic history. The interpolation procedure used in the Artemieva and Mooney study, however, causes mapped temperatures at 100-km depth to be up to $300^o$C or more higher outside the small region where heat flow data are available.

Temperatures estimated at a depth of 100 km attain highest values through the Tethysides belt and the variations correlate well with variations of $Q_o$ except throughout northern China and Mongolia where temperatures are similar to those throughout portions of northern Eurasia.

Temperatures beneath the Siberian traps stand out in Figure 12 as being just as high as those in parts of the Tethysides. The temperature anomaly appears as two southward extending arms, of which the eastern arm correlates well with the low $Q_o$ anomaly in Siberia and the location of the Siberian traps. The western arm lies slightly to the west of the $Q_o$ anomaly, but the disagreement is small enough to be explained by limitations in the resolvability of features (Figure 9) in the $Q_o$ and temperature maps.

### 6.3 Subducted lithosphere

Figure 13 shows temporal variations of volumes of subducted lithosphere at a depth of 300 km over the period 0-110 Ma as replotted from a global compilation (*Steinberger and O'Connell*, 1998). There appears to be a clear correlation between recent subducted lithosphere and low $Q$ values in the Tethysides but broad regions of low $Q$ to the north extend 2000 km or more northward from the northern extent of recent subduction in many regions. This subduction pattern indicates that an explanation of the low $Q_o$ values lying well northward of currently active subduction zones cannot be explained simply on the basis of high temperatures or upward percolation of fluids emanating from current and recently subducting lithosphere. This observation prompts us to propose either earlier subduction or other possible mechanisms for $Q_o$ variation in continental crust.

## 7 RELATION OF SPATIAL $Q_o$ VARIATIONS TO CRUSTAL PROPERTIES AND PROCESSES: SEISMIC VELOCITY, SEISMICITY AND STRAIN RATES

Available information related to crustal structure and processes that may be related to regional $Q_o$ variations include short-period seismic surface-wave group velocities, seismicity patterns and seismic strain rates for regions where that information is available.

### 7.1 Rayleigh-wave group velocities

*Ritzwoller and Levshin* (1998) mapped continent-wide Rayleigh- and Love-wave group velocities for periods of 20-100s across Eurasia. The maps exhibit greater small-scale variation than do upper mantle velocities, but in general, reflect the same features – low velocities for the Tethysides belt and generally higher values for northern Eurasia. They also are low in the Siberian Trap region (Fugure 1) where $Q_o$ (Figure 5) and upper mantle velocities (*Ekström and Dziewonski*, 1997) are low.

Particularly dense surface-wave group-velocity ($U_R$) coverage is available for the Arabian Peninsula (*Mokhtar et al.*, 2001). Dense coverage of *Lg* coda also allowed the determination of tomographic $Q_o$ and $\eta$ maps (*Cong and Mitchell*, 1998) with smaller cell size ($2^o$ x $2^o$) than our Eurasia-wide maps. Figure 14 compares the $Q_o$ map of *Cong and Mitchell* (1998) with

Rayleigh- wave group velocities of *Mokhtar et al.* (2001) at periods of 20-24 s. Although 100-s $C_R$ increases from west to east while $Q_o$ decreases, as discussed in the previous section, the shorter wavelength Rayleigh wave velocities decrease.

Both 1-Hz $Lg$ and 20-s $U_R$ predominantly sample crustal depths (Figure 11), so sediments, characterized by low seismic velocities and $Q_o$ values are the likely cause for both to decrease going from west to east. The increase with westward distance of 100-s $C_R$, on the hand, occurs because those waves in western Saudi Arabia predominantly sample the hot upper mantle and have relatively low velocities. As the crust thickens from west to east the upper mantle has a smaller effect on the 100-s waves, causing the velocity increase shown in Figure 10.

### 7.2 Seismicity and strain rates

Figure 15 maps epicenters of earthquakes that occurred between January 1, 2000 and April 30, 2003 for earthquakes with magnitudes of 4.5 and greater. All but a few of the events occurred in regions where $Q_o$ is less than about 500. Some regions, however, such as southeastern China and the Arabian Peninsula, where $Q_o$ is lower than 500, are marked by low levels of seismicity.

Regions of concentrated earthquake activity correspond with very low $Q_o$ values (<250) in four regions. One of these lies in western Turkey and extends with somewhat increasing values past the southern Caspian Sea. The entire region is seismically active, but especially so in the Aegean Sea and the westernmost portion of Turkey. *Jiménez-Munt et al.* (2003) found enhanced levels of crustal strain ($10^{-15} - 10^{-16}$) in that region. A map of the principal axes of model strain in western Turkey *Kreemer et al.* (2003) and determinations of surface velocity there with an eastern Turkey reference frame (*Zhu et al.*, 2006) show western Turkey to be undergoing north-south extensional strain.

A second concentrated region of very low $Q$ lies in the southern portion of the Tibetan Plateau and extends southward into Bhutan and easternmost India. Slightly higher $Q$ values (250-300) extend southeastward and include the Burma Trench where deep earthquakes occur. Both the $Q_o$ map of this study and that of *Mitchell et al.* (1997), delineate a region of low $Q$ values for $Lg$ coda in that region. *Xie* (2002), using direct $Lg$ waves with enhanced coverage and resolution for this region, found even lower $Q_o$ values in the southern Tibetan Plateau. *Kreemer et al.* (2003) report very high strain rates for this region with the highest rates occurring in the southern part of the region of lowest mapped $Q$ values in Figure 5.

A third region where $Q_o$ is low, although not quite as low as in the lowest-$Q$ portions of Tibet, lies just south of the Hindu Kush in Pakistan and India. This region, like that in southern Tibet, is marked by significant strain rates (*Kreemer et al.*, 2003).

A fourth very low-$Q$ zone lies in the Kamchatka Peninsula above a highly active subduction zone. The numerous large earthquakes that occur in that region (e.g. *Pollitz et al.*, 1998) suggest that the strain rate is quite high there.

The Zagros Fold Belt appears to be an exception to the rule that zones of lowest $Q_o$ coincide with zones high seismicity. That very active zone, characterized by many small earthquakes, lies in a region where $Q_o$ is between 300-350, values that are low but not as low as the four regions discussed above and no lower than in regions immediately outside the Zagros Fold Belt. *Masson et al.* (2005), in a combined analysis of the geodetic strain-rate field and the strain-rate field deduced from seismicity, found that seismic deformation in that region accounts for less

than 5 per cent of the total deformation. By contrast they found that seismic deformation comprises 30-100 per cent of total deformation in the Alborz-Kopet-Dag regions in northern Iran where several large earthquakes have occurred. Our results, when interpreted in light of the *Masson et al.* (2005) analysis suggest that regions exhibiting high levels of seismicity in a concentrated region may not be characterized by lower $Q$ values than its surroundings if most of the deformation there is due to geodetic strain and little to seismic strain. It is also interesting that crustal shortening in the Zagros has been found to occur as distributed thickening of the basement rather than by subduction processes (*Talebian and Jackson*, 2004). This would deprive that region of slab-generated crustal fluids that we postulate to be the cause of reduced $Q$ in continental crust.

# 8 SPATIAL $Q_o$ VARIATIONS AND THE TECTONIC EVOLUTION OF EURASIA

Both $Q_o$ and $\eta$ exhibit large spatial variations across Eurasia. Spatial variations of $Q_o$ show clear relationships to upper-mantle velocities, temperatures subducted lithosphere. All of these are deep-seated properties or processes that occur in the upper mantle of the Earth. Relationships of $\eta$ to the properties and processes that obviously affect $Q_o$ are, at the present time, not obvious and any relationship of that parameter to Earth processes will require further study when high-quality information is available for several of the Earth's continents. We will therefore, for the present, restrict our discussion to the regional variation of $Q_o$ and, for convenience, will present that discussion using two broad-scale types of feature – high-$Q$ platforms and low-$Q$ regions.

*Mitchell and Cong* (1998) selected several several high-$Q$ and low-$Q$ regions of the world where $Q_o$ was well determined over relatively broad areas and plotted those values as a function of the time elapsed since the most recent episode of tectonic or orogenic activity there. The present study has permitted us to add several points to that plot (Figure 16). All regions that are characterized by current or recent tectonic or orogenic activity have low $Q_o$ values while the most old shield or platform regions have high values. Regions where tectonic or orogenic activity occurred at intermediate times lie roughly along a line between those low and high values.

In this section we will discuss $Q_o$ determinations in several regions of Eurasia and show that spatial variations of $Q_o$ in almost every case are related to temporal occurrence of tectonic or orogenic activity there. We find it useful to divide this discussion into two major parts, platforms that almost, but not entirely, consist of high-$Q$ crust and low-$Q$ regions.

## 8.1 Platforms

The East European Platform is higher in $Q_o$ value (650-950) and broader in area than any other platform in northern Eurasia. Nonetheless much of the southern portion of that platform is marked by values much lower than those normally expected for a platform. These values are presumably associated with the subducting plate to the south that is responsible for the Tethysides belt.

Only the eastern portion of the Siberian (or Angara) Platform has platform-like $Q_o$ values (600-700). The western portion is marked by low $Q_o$ values that appear to be associated with

lower than expected upper mantle velocities (Figure 10) and higher than expected temperatures (Figure 12). The spatial correspondence between low crustal $Q$, high mantle temperatures and low mantle velocities in this region suggest that average crustal $Q$ as exemplified by $Q_o$ is strongly influenced by mantle processes that may have been prominent in the near or distant past.

The Khazakh Platform forms part the Altaid belt (Figure 1) and, according to maps in *Sengör and Natal'in* (1996), contains a higher proportion of cratonic and earliest Paleozoic (Cambrian - Silurian) rock than do other parts of the Altides. This composition may explain why $Q_o$ as well as suface-wave velocities (*Levshin et al.*, 2005) are higher there than in surrounding regions. *Sarker and Abers* (1999) measured $Q$ for higher frequency (8-12 Hz) seismic waves in that region and also found that it was higher than in nearby mountainous regions.

The Arabian Peninsula, although consisting of a shield in its westernmost portions and a platform for most of the rest of its area, is chacterized by surprisingly low $Q_o$ values (Figure 14) for a stable region. $Q_o$ in the shield is 400-450 and decreases to about 350 in much of its eastern regions. An exception is the Oman Fold Belt in the southeastern corner of the Peninsula where $Q_o$ is as low as about 250. *Kusky and Robinson* (2005) have mapped Tertiary faulting in the region that indicates recent tectonic activity.

The map of estimated temperatures at a depth of 100 km (Figure 12) shows temperature in the Arabian Peninsula varying between about 850 and $1250^o$. As discussed earlier this distribution results from the method of smoothing in determining the temperature distribution. The slowly varing $Q_o$ values, likely due to increasing thicknesses of low-$Q$ sediments from west to east, suggest a much more uniform temperature field beneath Saudi Arabia. The heat flow determinations made in Saudi Arabia (*Gettings et al.*, 1986) are typical of stable crust. Mantle temperatures determined by geochemical means indicate that upper mantle temperatures beneath the Arabian Peninsula are 300-$400^o$ higher than those further to the west. This disparity between upper mantle temperatues and crustal temperatures suggests that a factor, other than temperature is responsible for the relatively low $Q$ values observed across Saudi Arabia. This difference, we believe, can be explained by a non-equilibrium situation in which the relatively low $Q_o$ values in the Arabian Peninsula are produced by fluids that have been released in the upper mantle by hydrothermal processes and have traveled upward from the that deep source at faster rate than the heat from it.

## 8.2 Low-$Q$ regions

In this sub-section we will discuss the low $Q_o$ values in the Tethysides belt as well as in regions where we found $Q_o$ to be unexpectedly low. The Tethysides contain some of the lowest $Q$ regions in the world. They include portions of western Turkey, the Hindu Kush region and southeastern Tibet where, as discussed in the section on crustal properties and $Q_o$ variations, seismicity rates are very high. In those three regions, as well as Kamchatka, the low $Q_o$ appear to be related to be related to high levels of crustal strain there.

Except for a gap of a few hundred miles in northern India, estimated 100-s Rayleigh-wave phase velocities (Figure 10) are low in the same regions of the Tethysides where $Q_o$ is low. Likewise, temperatures at a depth of 100 km (Figure 12) closely resemble the Tethysides $Q_o$ distribution everywhere except northern China where they are 200-$300^o$ cooler than temperatures south and west from there. The relatively low $Q_o$ values in that region could perhaps be exlained

by the same mechanism that we propose for the Arabian Peninsula (i.e. fluids from an upper mantle heat source travel to the crust at a faster rate than does heat from that source). But other mechanisms, such as those discussed in the following section, could also be viable possibilities.

$Q_o$ in England and the portions of mainland Europe to the east seem unusually low for regions with such low levels of tectonic activity. Our values for $Q_o$ there (about 250-350) are close to those obtained by *Baqer and Mitchell* (1998) and others for California and the western part of the Basin and Range province in the United States ( 275). The $Q_o$ values are consistent with equations used to obtain magnitudes in Britain (*Booth*, 2005) which are same as those used for determining magnitudes in California (*Hutton and Boore*, 1987). Also, a detailed study in France (*Campillo et al.*, 1985) yields values of about 350. Both of those results are consistent with the relatively low $Q_o$ determinations in those regions in our continent-wide map.

Another interesting region with low $Q_o$ values lies in Oman, in the southeastern corner of the Arabian Peninsula. Those values, as low as about 250, when compared to Figure 16, suggest recent tectonic or orogenic activity in that region. *Searle and Cox* (2002), in a study of metamorphism in the Oman Mountains, find evidence for high-temperature obduction during late Cretaceous time (70-95 Ma). A $Q_o$ value of 250 appears to be too low to be consistent with the time predicted by Figure 16. *Kusky and Robinson* (2005), however, have found Quaternary uplift in that region which they propose lies on the active forebulge of a collision zone between the NE margins of the Arabian plate, the Zagros fold belt and an accretionary prism. If their proposal is correct, our $Q_o$ values in that region are consistent with the $Q_o$ - Time plot. There is, however, also the possibility that our $Q_o$ determinations in that region may be too low because of insuffucient data coverage to provide precise values near the continental boundaries.

# 9 RAYLEIGH-WAVE ATTENUATION

As indicated earlier $Lg$ coda $Q$ is typically described by the expression $Q_o f^{\eta}$. Figures 5 and 6 present maps, respectively, of $Q_o$ and $\eta$ for the entire Eurasian continent. Our goal, in this section, is to use the mapped values of $Q_o$ and $\eta$ to develop maps of Rayleigh-wave attenuation coefficients ($\gamma_R$) at selected periods for all of Eurasia. These coefficients control the attenuation of Rayleigh wave amplitudes as described by the expression $A = A_o e^{-\gamma x}$ where $A_o$ is a reference amplitude, and $x$ is distance traveled by the Rayleigh wave. Before developing the maps we anticipated that they would resemble the $Q_o$ maps for $Lg$ waves with regions of high $\gamma_R$ roughly coinciding with regions of low $Q_o$ and vice versa. Some departures from this relationship are, however, expected to occur because of regional variations in the frequency dependence of shear-wave $Q$ ($Q_\mu$). Also, it is reasonable to expect that attenuation coefficient values will differ significantly from one period to another with $\gamma_R$ values at shorter periods being higher than those at longer periods.

## 9.1 Methodology

We begin by assuming that we can calculate those coefficients using estimated values of (1) average shear-wave $Q$ ($Q_\mu$) in the crust in the region of interest and (2) the values of the frequency dependence of $Q_\mu$ ($\zeta$), as a function of depth in that region. Knowing those values we can then use standard methods for computing $\gamma_R$. In order to calculate $\gamma_R$ we, in addition

to knowing shear- and compressional-wave $Q$ values, must know both shear- and compressional-wave velocity values. The velocity information is available from the global model of *Laske et al.* (2001). We chose values that are appropriate for each cell of our $Q_o$ and $\eta$ maps in Figures 5 and 6.

Some studies of $Lg$ attenuation (e.g. *Herrmann and Kijko*, 1983; *Campillo*, 1987) indicate that 1-Hz $Q_{Lg}$ provides a good approximation for average shear-wave $Q$ ($Q_\mu$) in the continental crust. We therefore use values of $Q_o$ in Figure 5 to approximate average $Q_\mu$ for the crust and continue that value into the uppermost mantle. If we can then devise a way to estimate how the frequency dependence factor $\eta$ for $Q^C_{Lg}$ relates to the frequence-dependence factor ($\zeta$) for $Q_\mu$ we should be able to determine Rayleigh-wave attenuation ($\gamma_R$) for every cell in our Eurasian map where we have previously determined values for $Q_o$ and $\eta$.

Our next step is, therefore, development of an empirical method for estimating $\zeta$ for each cell. We quickly learned that simply using the measured value of $\eta$ in Figure 6 would not work. In order to find an appropriate $\zeta$ model we found several paths in Eurasia, mostly in the southern part, where $\gamma_R$ had been determined using two-station paths. All of the paths lie in either the Middle East (*Cong and Mitchell*, 1998) or China (*Jemberie and Mitchell*, 2004). Those paths provide a sufficiently large data base to enable us to develop an empirical relation between $\eta$ (the frequency dependence of $Q^C_{Lg}$) at 1 Hz and the depth variation of $\zeta$ (the frequency dependence of $Q_\mu$).

We sought a depth-variable factor with which we could multiply $\eta$ that would provide us with an apparent $\zeta$ distribution with depth that would be consistent with the $Q_o$ and $\eta$ values of Figures 5 and 6 at 1 Hz and allow us to empirically fit computed values of $\gamma_R$ to observed values at periods between 5 and 50 s. Satisfactory fits for most of our sets of observed $\gamma_R$ values were produced if we multipled $\eta$ by 0.5 for depths between 0 and 40 km and by 0.8 at greater depths. This depth-variable factor, when multiplied by $\eta$ provides us with an apparent $\zeta$ distribution that explains $Lg$ coda $Q$ and its frequency dependence as well as Rayleigh-wave attenuation coefficients at periods between 5 and 50 s.

Figure 17 compares the $\gamma_R$ variation with period that we obtained using our empirical method and average measured $\gamma_R$ values for paths between an event in central China and station pairs YSS-HIA and YSS-MDJ. The agreement between predicted and observed $\gamma_R$ curves for this case is excellent, as are several other cases that we tested. Some cases differ significantly only for the the shortest period ($\sim$5 s) and other differ slightly for all periods. For one case the observed $\gamma_R$ curve exhibits much greater attenuation than predicted for all periods. That case was for a path near the southern end of Lake Baikal where $Q_o$ and $\eta$ standard errors (Figures 7 and 8) are very large and suggest a region of anomalous wave propagation.

### 9.2 Rayleigh-wave attenuation maps for Eurasia

Figures 18-21 are maps of Rayleigh-wave attenuation coefficients for periods of 5, 10, 20 and 50 s that we obtained using the method described above when we assumed that compressional-wave $Q$ ($Q_\alpha$) is twice as large as shear-wave $Q$ ($Q_\mu$). Figures 22-25 are maps for the same periods but were obtained assuming that $Q_\alpha = Q_\mu$.

Comparison of the two sets of maps indicates that our choice of $Q_\alpha/Q_\mu$ had almost no effect on the resulting $\gamma_R$ maps at periods of 5 and 10 s whereas at 20s and 50s differences are more

obvious. All maps bear at least some resemblance to the 1-Hz $Q_o$ map in Figure 5 over most of their areas, especially the 20-s and 50-s maps. This result is reasonable since we know that the $Lg$ phase consists of many higher Rayleigh modes that sample the entire crust. Crustal properties over that same depth range also primarily control 20 and 50 s fundamental-mode Rayleigh waves whereas properties of the upper crust primarily control 5 and 10 s fundamental-mode Rayleigh waves. Moreover, sedimentary basins that appear as small regions of high attenuation on the 10 s map, and especially the 5 s map, are not evident on either the 20 s or 50 s map.

Both 5-s Rayleigh-wave attenuation coefficient maps (Figures 18 and 22) show values that range from about 0.5 to 5 x $10^{-3}$ $km^{-1}$. They display a nearly continuous southward convex arc of low attenuation stretching from Scandinavia to northeastern Siberia. Unlike the $Q_o$ map it dips slightly south of Lake Baykal. Several small regions of high attenuation lie both to the north and south of that arc. A check the Laske et al. velocity tabulation indicate that they correspond to thick accumulations of sediment. The two largest ones appear to be those associated with the Barents/Karal and Black Seas. Other regions of low attenuation lie in India and the western portion of the Arabian Peninsula.

Values in both 10-s Rayleigh-wave attenuation coefficient maps (Figures 19 and 23) vary between 0.2 and 2.2 x $10^{-3}$ $km^{-1}$. They show the same southward arcing band of high values that appeared on the 5-s map. The portion of the arc that was south of Lake Baykal has now migrated slightly northward. The arc for the case $Q_\alpha = Q_\beta$ is, like the $Q_o$ map beginning to become segmented. Since the wavelengths of these waves are much larger than those for the 5-s waves, only the larger sedimentary basins appear on this map. High attenuation coefficients associated with the Siberian traps are beginning to emerge and low attenuation values now cover almost all of India.

20-s Rayleigh-wave attenuation coefficients (Figures 20 and 24) vary between about 0.1 and 1.1 x $10^{-3}$ $km^{-1}$. The arc of low attenuation is now distinctly segmented with three principal regions of low values. A clear southern zone of high attenuation with four concentrations of especially high attenuation now extends from Spain to central China. A clear appearance of increasing attenuation from west to east now appears in the Arabian Peninsula. Attenuation continues to be low throughout most of India. The Siberian Trap high-attenuation zone is now seen clearly and covers a large region in north-cental Siberia. It extends well into the Kara Sea where it is probably covered by sediments and is thus unmapped by geologists. Some features stand out more strongly in the 20-s $\gamma_R$ maps than in the $Q_o$ map. Particularly noticeable are the Siberian trap region of north-central Siberia and central portions of the four low-Q cratonic regons.

50-s Rayleigh-wave attenuation coefficient values (Figures 21 and 25) range between about 0.06 and 0.30 x $10^{-3}$ $km^{-1}$. The patterns in these maps look much like those in the 20-s maps, but concentrations of both high- and low-attenuation tend to take on somewhat higher and lower values, respectively, than the 20-s maps and cover a somewhat broader area. This, presumably, occurs because the 50-s waves sample a greater depth range in the upper mantle where our ability to resolve small features is smaller than it is for 20-s waves.

# 10 CONCLUSIONS

A new set of 1-Hz $Lg$ coda $Q$ determinations across Eurasia nearly quaduples that of an earlier study. It provides new information on the spatial variation of $Q_o$ and $\eta$ across virtually the entire Eurasian continent in which $Q_o$ varies between 200 or less and nearly 1000 and $\eta$ varies between 0.3 and 1.0.. The variation of $Q_o$, which represents an average estimate of shear-wave $Q$ variation is, in most regions, directly proportional to upper mantle shear-wave velocity variation and inversely proportional to upper mantle temperature variatons over broad areas. In the crust it is also directly proportional to shear-wave velocities and exhibits lowest values in regions where seismicity is concentrated and high and crustal strain is also high.

The four regions of highest $Q_o$ occur in the East European, Siberian, Kazakh and Indian platforms. Within the Siberian and Indian platforms, however, lower than expected values occur, apparently being related to upper mantle heat sources that are readily seen in maps of 100-s Rayleigh- wave phase velocities and estimated temperatures a depth of 100 km.

The Tethysides belt, a broad region of low $Q_o$ extends from western Europe eastward to easternmost Asia. Most of those low $Q_o$ values lie in regions that also are marked by low values of 100-s Rayleigh-wave velocities, high temperatures and, often, subducted lithospere.

We developed the first continent-wide maps of Rayleigh-wave attenuation for Eurasia. Because $Q_{Lg}^C$ varies with frequency $Q_o$ cannot be used alone to infer Rayleigh-wave attenuation at lower frequencies. In addition, since the frequency-dependence parameter ($\eta$) of $Q_{Lg}^C$ varies regionally, between 0.3 and 1.0, with no predictable pattern of variation it is not feasible to assume a single value for the $Q$ frequency dependence to attempt to predict patterns of Rayleigh-wave attenuation. We developed an empirical relation between the frequency-dependence parameter of $Lg$ coda $Q$ at 1 Hz and the frequency-dependence parameter of $Q_\mu$ that allowed us to map Rayleigh-wave attenuation coefficient variation across all of Eurasia for the first time. 5-s, 10-s, 20-s and 50-s Rayleigh-wave attenuation coefficients vary, respectively, between about 0.5 and 5.0 x $10^{-3}$ km$^{-1}$, 0.2 and 2.2 x $10^{-3}$ km$^{-1}$, 0.1 and 1.1 x $10^{-3}$ km$^{-1}$, and 0.06 and 0.3 x $10^{-3}$ km$^{-1}$. Rayleigh-wave attenuation coefficients ($\gamma_R$) at short periods (5 and 10 s) are dominated by small-scale sedimentary features while longer-period waves are insensitive to those features. Variations shown by the $\gamma_R$ maps, especially those for 20- and 50-s periods, show many similarities to, but also some significant differences from, the variations of our $Q_o$ map for $Lg$ coda.

## 11 REFERENCES


Artemieva, I. M., and W. D. Mooney (2001), Thermal evolution of Precambrian lithosphere; a global study, *J. Geophys. Res.*, *106*, 16,387–16,414.

Artemieva, I. M., M. Billien, J.-J. Lèvêque, and W. D. Mooney (2004), Shear-wave velocity, seisic attenuation, and thermal structure of the continental upper mantle, *Geophys. J. Int.*, *157*, 607–628.

Baqer, S., and B. J. Mitchell (1998), Regional variation of $Lg$ coda $Q$ in the continental United States and its relation to crustal structure and evolution, *Pure Appl. Geophys.*, *153*, 613–638.

Baumgardt, D. R. (2001), Sedimentary basins and the blockage of $Lg$ wave propagation in the continents, *Pure Appl. Geophys.*, *158*, 1207–1250.

Booth, D. C. (2005), Distance and station effects on UK shear- and Lg-wave amplitudes, *Geophys. J. Int.*

Bowman, J. R., and B. L. N. Kennett (1991), Propagation of $Lg$ waves in the North Australian craton: Influence of crustal velocity gradients, *Bull. Seismol. Soc. Am.*, *81*, 592–610.

Campillo, M. (1987), $lg$ propagation in a laterally varying crust and the distribution of the apparent quality factor in central europe, *J. Geophys. Res.*, *92*, 12,604–12,614.

Campillo, M., J.-L. Plantet, and M. Bouchon (1985), Frequency-dependent attenuation in the crust beneath central France from $Lg$ waves: Data analysis and numerical modeling, *Bull. Seismol. Soc. Am.*, *75*, 1395–1411.

Cong, L., and B. J. Mitchell (1998), $Lg$ coda $Q$ and its relation to the geology and tectonics of the Middle East, *Pure Appl. Geophys.*, *153*, 563–585.

Dziewonski, A. M., and D. L. Anderson (1981), Preliminary reference Earth model (PREM), *Phys. Earth Planet. Inter.*, *2*, 297–356.

Ekström, G., and A. M. Dziewonski (1997), The unique anisotropy of the Pacific upper mantle, *Nature*, *394*, 168–172.

Gettings, M. E., J. H. R. Blank, W. D. Mooney, and J. H. Healey (1986), Crustal structure of southwestern Saudi Arabia, *J. Geophys. Res.*, *91*, 6491–6512.

Gordon, R. (1974), A tutorial on art, *IEEE Trans. Nucl. Sci.*, *NS-21*, 78–93.

Gordon, R. G., and D. Jurdy (1986), Cenozoic plate motions, *J. Geophys. Res.*, *91*, 12,389–12,406.

Gregersen, S. (1984), $Lg$-wave propagation and crustal structure differences near Denmark and the North Sea, *Geophys. J. R. astr. Soc.*, *79*, 217–234.

Herrmann, R. B., and A. M. Kijko (1983), Modeling some empirical vertical component $lg$ relations, *Bull. Seismol. Soc. Am.*, *73*, 157–171.

Humphreys, E., and R. W. Clayton (1988), Adaptation of back projection tomography to seismic travel time problems, *J. Geophys. Res.*, *93*, 1073–1086.

Hutton, L. K., and D. M. Boore (1987), The $M_L$ scale in southern California, *Bull. Seismol. Soc. Am.*, *77*, 2074–2094.

Jemberie, A. L., and B. J. Mitchell (2004), Shear-wave $Q$ structure and its lateral variation in the crust of China and surrounding regions, *Geophys. J. Int.*, *157*, 363–380.

Jiménez-Munt, I., R. Sabadini, and A. Gardi (2003), Active deformation in the Mediterranean from Gibraltar to Anatolia inferred from numerical modeling and geodetic and seismological data, *J. Geophys. Res.*, *2006*, doi:10.1029/2001JB001,544.

Kadinsky-Cade, K., M. Barazangi, J. Oliver, and B. Isaaks (1981), Lateral variations of high-frequency seismic wave propagation at regional distances across the Turkish and Iranian plateaus, *J. Geophys. Res.*, *86*, 9377–9396.

Kennett, B. L. N., S. Gregersen, S. Mykkeltveit, and R. Newmark (1985), Mapping of crustal heterogeneity in the North Sea basin via the propagation of $Lg$-waves, *Geophys. J. R. astr. Soc.*, *83*, 299–306.

Kreemer, C., W. E. Holt, and A. J. Hanes (2003), An integrated global model of present-day motions and plate boundary deformation, *Geophys. J. Int.*, *154*, 8–34.

Kusky, T. M., and C. Robinson (2005), Tertiary-quaternary faulting and uplift in the northern Oman Hajar mountains, *J. Geol. Soc. London*, *i1*, submitted.

Laske, G., G. Masters, and C. Reif (2001), *A new global crustal model at 2x2 degrees*, http://mahi.ucsd.edu/Gabi/rem.html.

Levshin, A. L., M. H. Ritzwoller, and N. M. Shapiro (2005), The use of crustal higher modes to constrain crustal structure across central Asia, *Geophys. J. Int.*, *160*, 961–972.

Lithgow-Bertelloni, C. (1994), The history and dynamics of plate motions, Ph.d. diss., Univ. California, Berkeley.

Malin, P. E. (1978), A first-order scattering solution for modeling lunar and terrestrial seismic coda, Ph.d. diss., Princeton Univ.

Masson, F., J. Chéry, D. Hatfield, J. Martinod, P. Vernant, F. Tavakoli, and A. Ghafory-Ashtiani (2005), Seismic versus aseismic deformation in Iran inferred from earthquakes and geodetic data, *Geophys. J. Int.*, *160*, 217–226.

McMechan, G. A. (1983), Seismic tomography in boreholes, *J. Geophys. Res.*, *74*, 601–612.

Mitchell, B. J., and L. Cong (1998), $Lg$ coda $Q$ and its relation to the structure and evolution of continents: A global perspective, *Pure Appl. Geophys.*, *153*, 655–663.

Mitchell, B. J., and H. J. Hwang (1987), Effect of low-$Q$ sediments and crustal $Q$ on $Lg$ attenuation in the United States, *Bull. Seismol. Soc. Am.*, *77*, 1197–1210.

Mitchell, B. J., Y. Pan, J. Xie, and L. Cong (1997), *Lg* coda *Q* variation across Eurasia and its relation to crustal evolution, *J. Geophys. Res.*, *102*, 22,767–22,779.

Mokhtar, T. A., C. J. Ammon, R. B. Herrman, and H. A. A. Ghalib (2001), Surface-wave velocities across Arabia, *Pure Appl. Geophys.*, *158*, 1425–1444.

Pollitz, F. F., R. Bürgmann, and B. Romanowicz (1998), Viscosity of oceanic asthenosphere inferred from remote triggering of earthquakes, *Science*, *280*, 1245–1249.

Reichow, M. K., A. D. Saunders, R. V. White, M. S. Pringle, A. I. Al'Mukhamedov, A. I. Medvedev, and N. P. Kirda (2002), $^{40}$ar/$^{39}$ar dates from the West Siberian Basin: Siberian flood basalt province doubled, *Science*, *296*, 1846–1849.

Ritzwoller, M., and A. L. Levshin (1998), Eurasian surface-wave tomography: Group velocities, *J. Geophys. Res.*, *1103*, 4839–4878.

Sandvol, E. K., K. Al-Damegh, A. Calvert, D. Seber, M. Barazangi, R. Mohamad, R. Gök, N. Türkelli, and C. Gürbüz (2001), Tomographic imaging of *Lg* and *Sn* propagation in the Middle East, *Pure Appl. Geophys.*, *158*, 1121–1163.

Sarker, G., and G. A. Abers (1999), Lithospheric temperature estimates from seismic attenuation across range fronts in southern and central Eurasia, *Geology*, *27*, 427–430.

Searle, M. P., and J. Cox (2002), Subduction zone metamorphism during formation and emplacement of the Semail ophiolite in the Oman Mountains, *Geo. Mag.*, *139*, 241–255.

Sengör, A. M. C. (1984), The Cimmeride orogenic system and the tectonics of Eurasia, *Spec. Paper Geol. Soc. Am.*, *195*, 213–244.

Sengör, A. M. C. (1987), Tectonics of the Tethysides: Orogenic collage development in a collision setting, *Ann. Rev. Earth Planet. Sci.*, *15*, 213–244.

Sengör, A. M. C., and B. A. Natal'in (1996), Paleotectonics of Asia: Fragments of a synthesis, in *The Tectonic Evolution of Asia*, edited by A. Yin and M. Harrison, pp. 486–640, Cambridge Univ. Press.

Sengör, A. M. C., B. A. Natal'in, and V. S. Burtman (1993), Evolution of the Altaid tectonic collage and Paleozoic crustal growth in Eurasia, *Nature*, *364*, 299–307.

Steinberger, B., and R. J. O'Connell (1998), Advection of plumes in mantle flow: Implications for hotspot motion, mantle viscosity and plume distribution, *Geophys. J. Int.*, *132*, 412–434.

Talebian, M., and J. Jackson (2004), A reappraisal of earthquake focal mechanisms and active shortening in the Zagros mountains of Iran, *Geophys. J. Int.*, *156*, doi:10.111/j.1365–246X.2004.02,092.x.

Xie, J. (2002), *Lg Q* in the eastern Tibetan Plateau, *Bull. Seismol. Soc. Am.*, *92*, 871–876.

Xie, J., and B. J. Mitchell (1990a), Attenuation of multiphase surface waves in the Basin and Range province, I. *Lg* and *Lg* coda, *Geophys. J. Int.*, *102*, 121–127.

Xie, J., and B. J. Mitchell (1990b), A back-projection method for imaging large-scale lateral variations of *Lg* coda *Q* with application to continental Africa, *Geophys. J. Int.*, *100*, 161–181.

Xie, J., and O. W. Nuttli (1988), Interpretation of high-frequency coda at large distances: Stochastic modeling and method of inversion, *Geophys. J.*, *95*, 579–595.

Zhang, T., and T. Lay (1994), Analysis of short-period regional phase path effects associated with topography in Eurasia, *Bull. Seismol. Soc. Am.*, *84*, 119–132.

Zhu, L., N. Akyol, B. J. Mitchell, and K. Kekovali (2006), Seismotectonics of western Turkey from high-resolution earthquake relocations and moment tensor determinations, *Geophys. Res. Lett.*, *33*, L07,316,doi:10.1019/2006GL025,842.

Ziegler, P. A. (2005), Permian to recent evolution, in *Encyclopedia of Geology*, edited by R. C. Selley, S. R. M. Cocks, and I. R. Palmer, pp. 102–125, Elsevier, Philadelphia.

Zonenshain, L. P., M. I. Kuzmin, and L. M. Natapov (1990), *Geology of the USSR: A plate-tectonic synthesis*, 242 pp., AGU, Washington, DC.

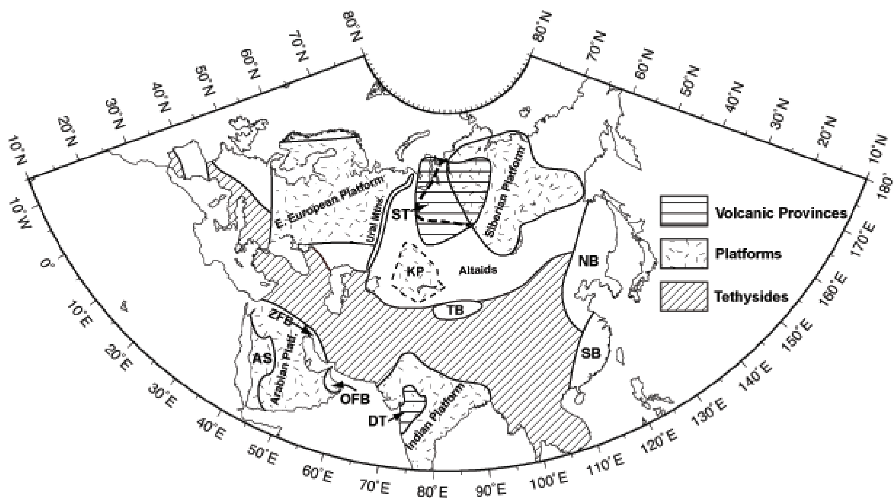


Figure 1: Simplified tectonic map of Eurasia. The Tethysides complex is modified from *Sengör* (1984). AS = Arabian Shield, DT = Deccan Traps, KP = Kazakh Platform, NB = Northeast China Block, OFB = Oman Fold Belt, SB = Southeast China Block, ST = Siberian Traps, TB = Tarim Block and ZFB = Zagros Fold Belt. The solid line surrounding the Siberian Traps delineates the maximum area and the dashed line delineates the minimum area of the Siberian Traps as inferred by *Reichow et al.* (2002).

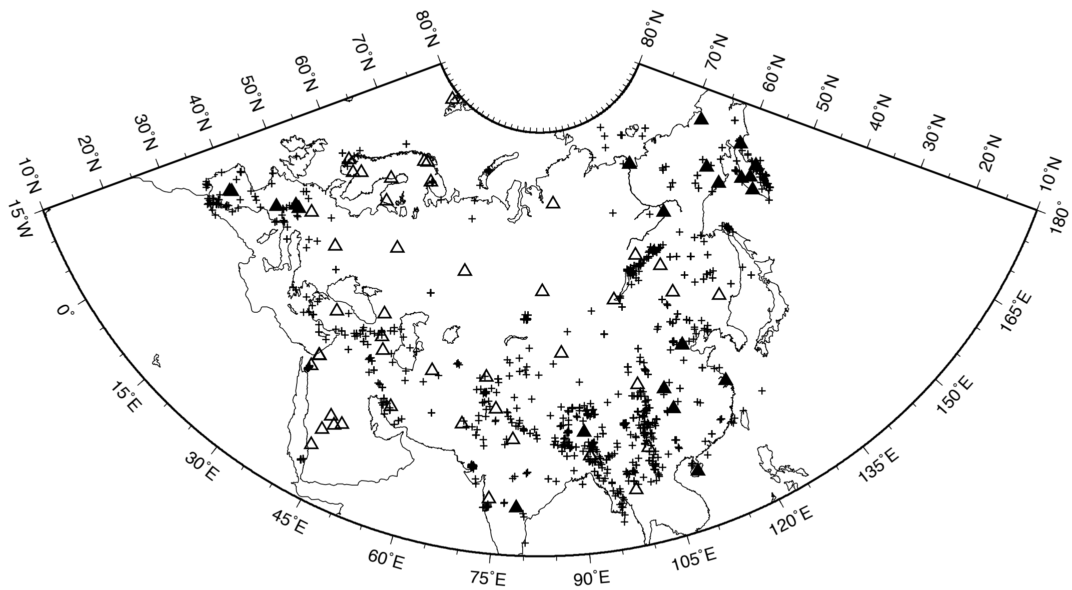


Figure 2: Map of earthquakes (+) and stations ($\Delta$). Filled symbols denote stations that are new to this study and open symbols denote stations used in earlier work (*Mitchell et al.*, 1997)
.

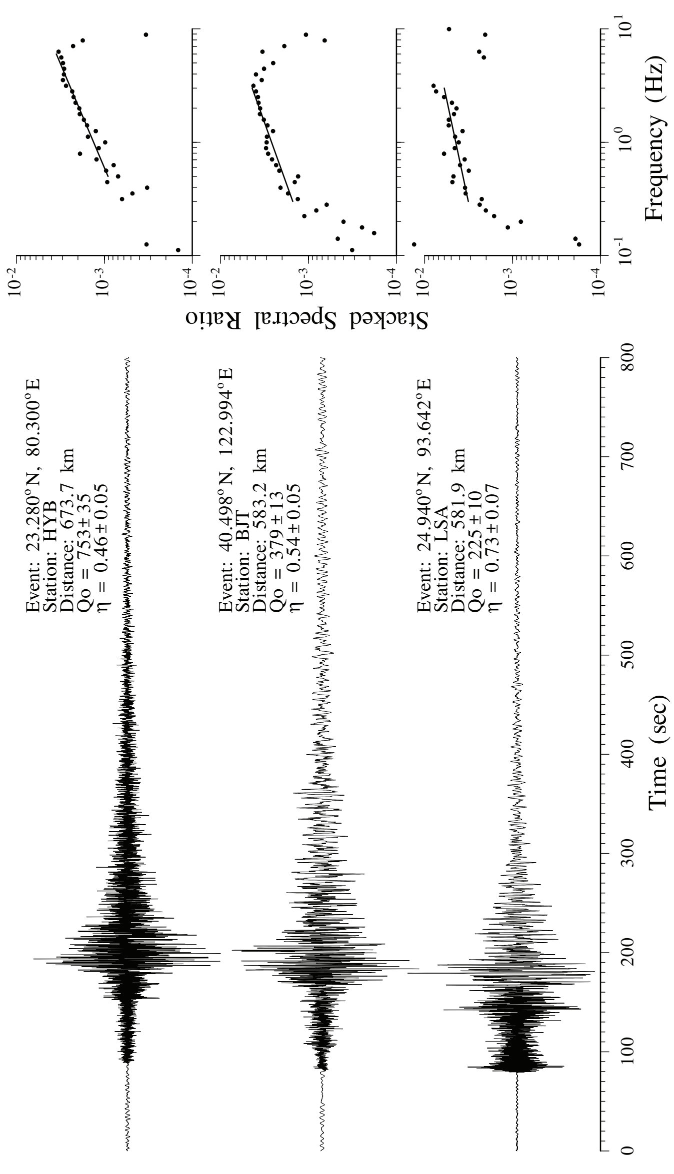


Figure 3: Left - Comparison of seismograms recorded for a relatively high-$Q$ (701) path to station HYB in India, for a relatively low-$Q$ (359) path to station BJT in northeastern China, and for a very low-$Q$ (208) path to station LSA in Tibet. Right - Stacked Spectral Ratio plots (SSR's) corresponding the three seismograms.

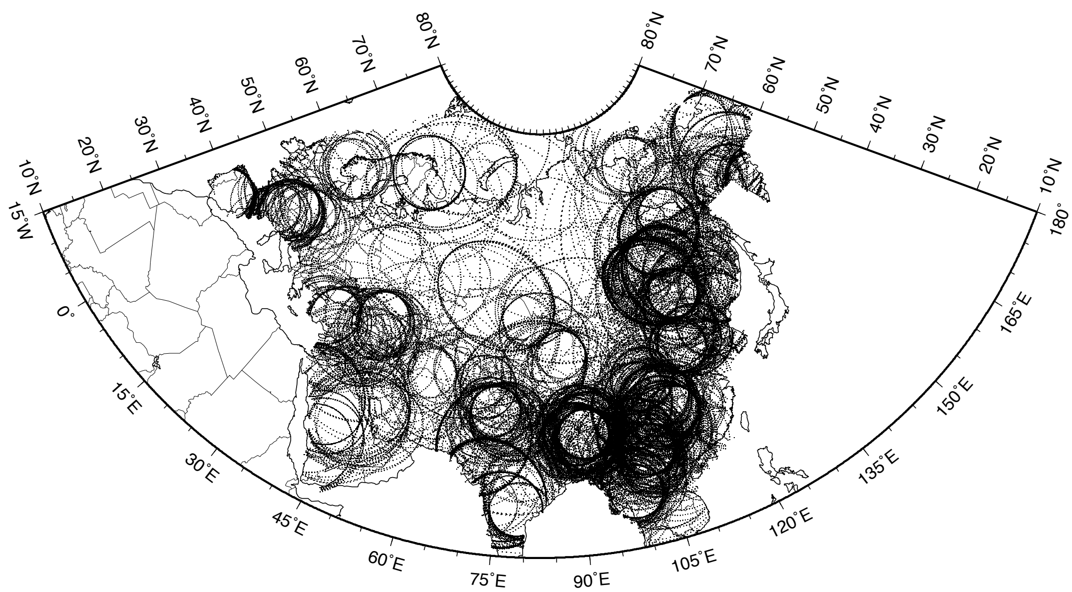


Figure 4: Assumed sampling patterns, or scattering ellipses, for late *Lg* coda in this study. The ellipses are assumed to represent areas sampled at the maximum lapse times used in the analysis of each seismogram. Since *Lg* does not propagate through oceanic structure ellipses are truncated at continental boundaries.

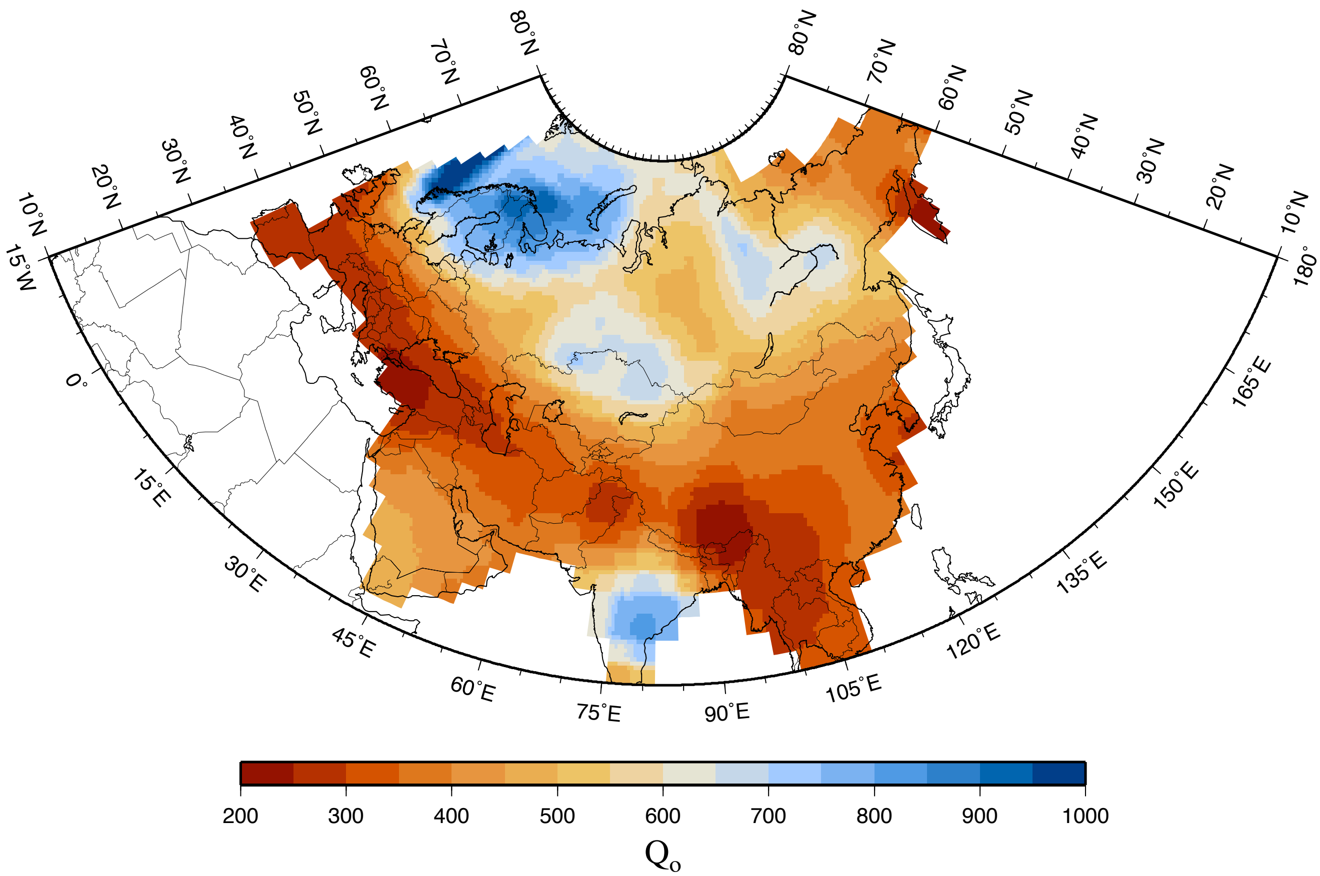


Figure 5: Tomographic map of $Q_o$ at 1 Hz for Eurasia. Each cell is $3^o$ x $3^o$ in area.

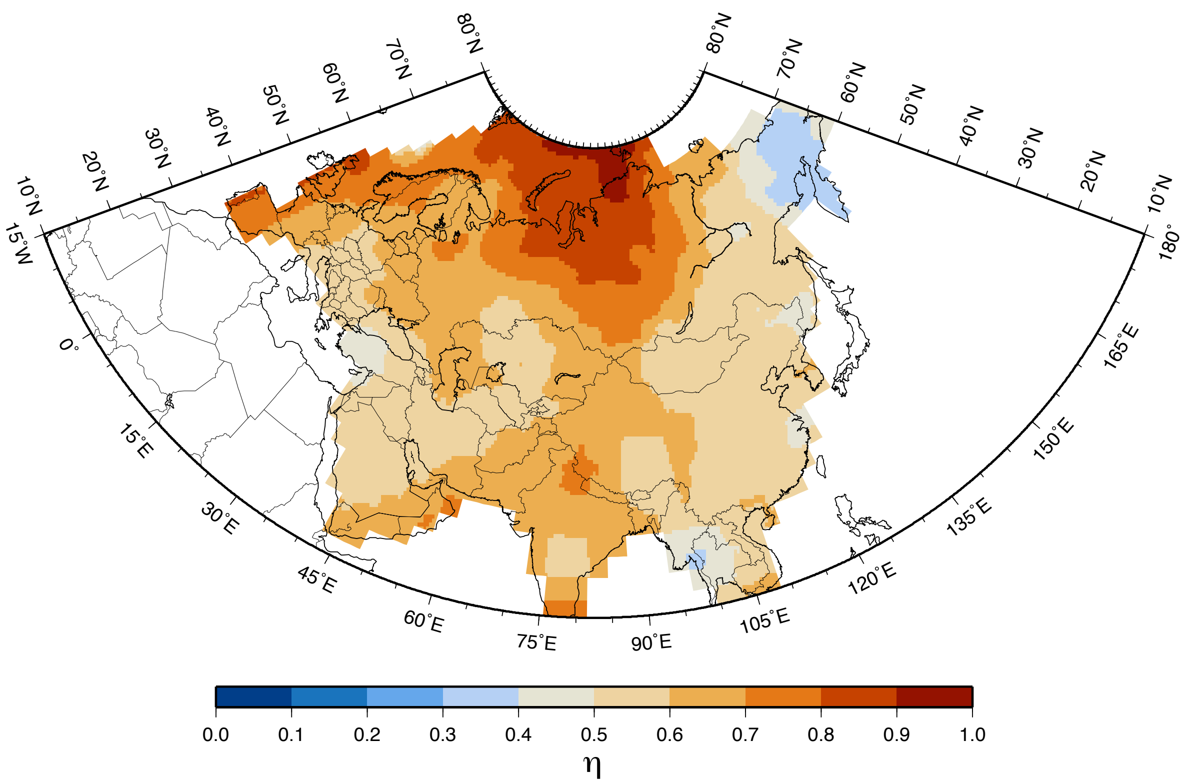


Figure 6: Tomographic map of the frequency dependence ($\eta$) of $Q_{Lg}^{C}$ at 1 Hz for Eurasia. Each cell is $3^o$ x $3^o$ in area.

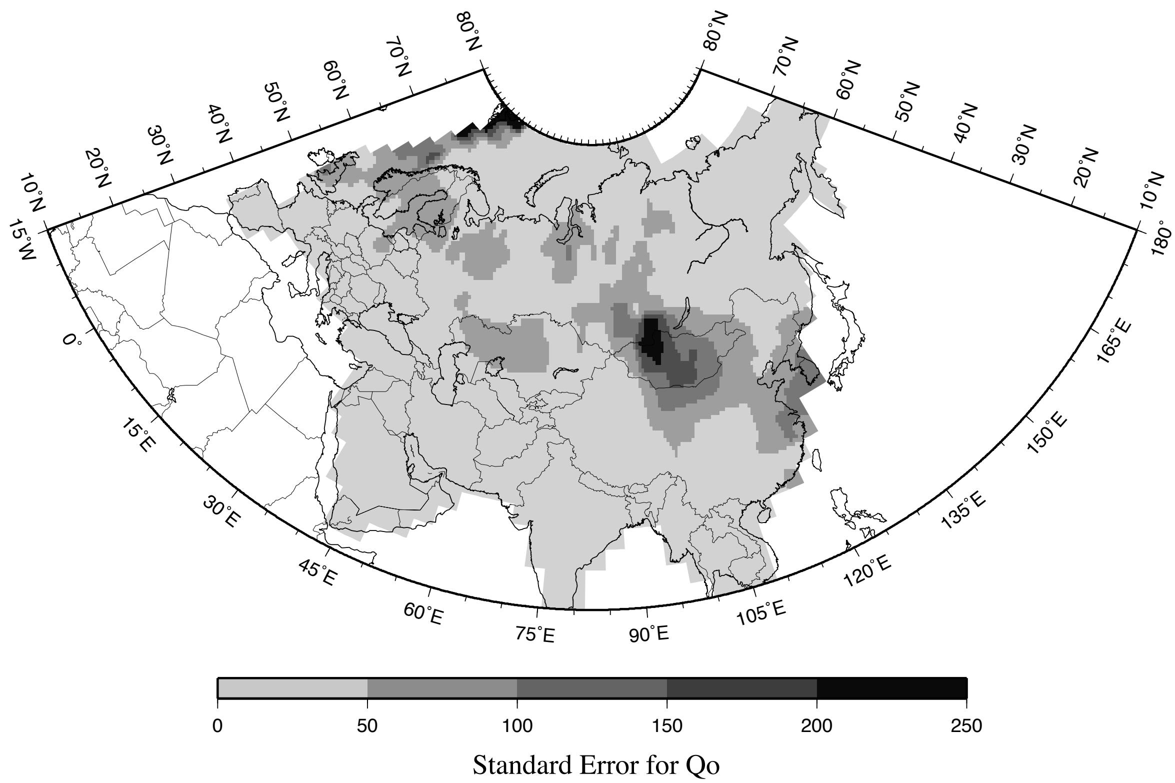


Figure 7: Map of standard errors for $Q_o$ in Eurasia.

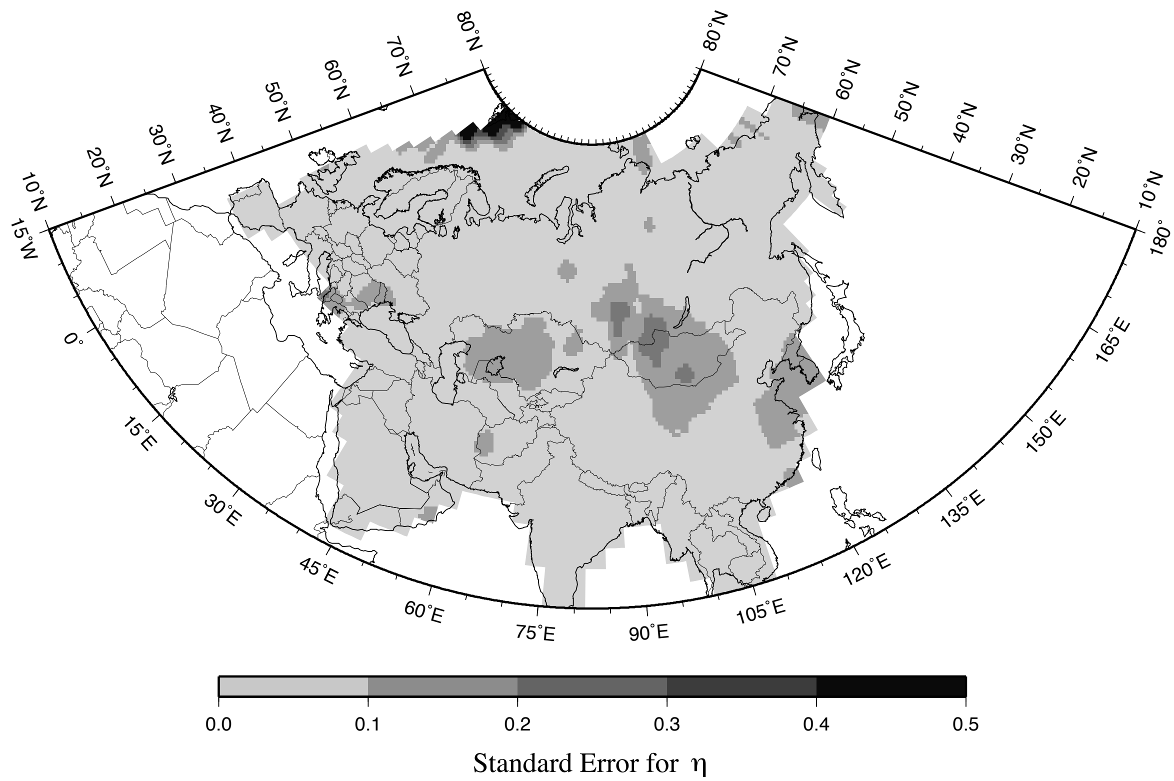


Figure 8: Map of standard errors for $\eta$ in Eurasia.

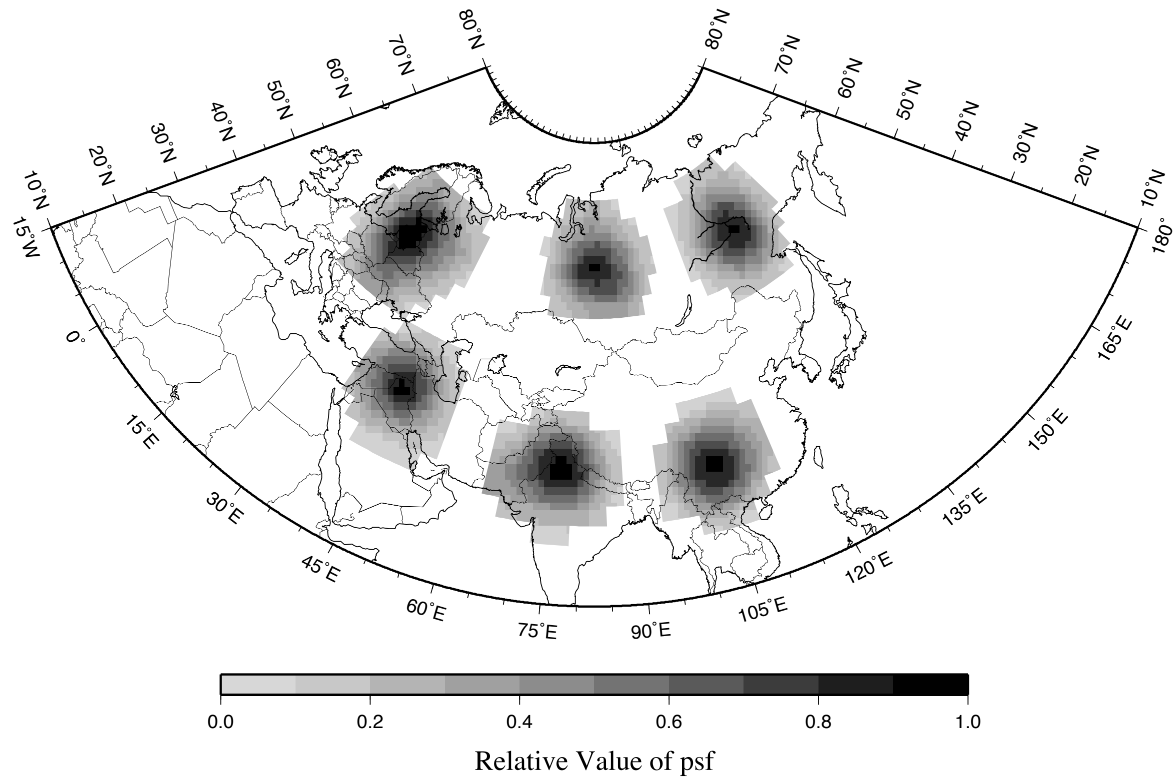


Figure 9: Point spreading function ($psf$) plots for six selected cells.

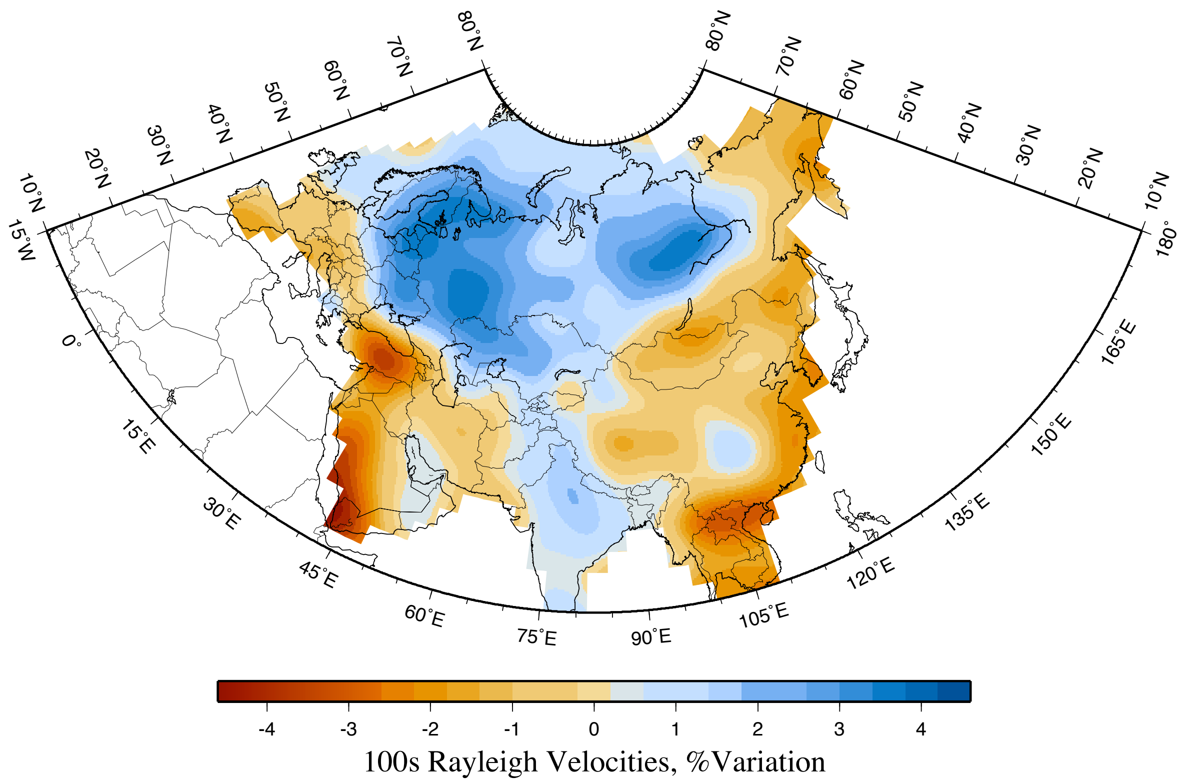


Figure 10: Map of Rayleigh-wave phase velocities at a period of 100s for Eurasia (adapted from *Ekström and Dziewonski* [1997]).

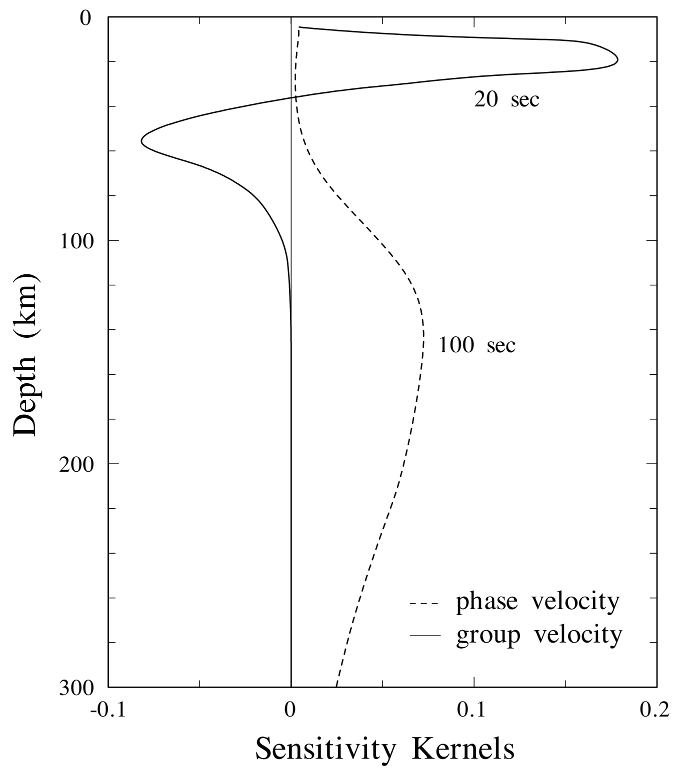


Figure 11: Sensitivity kernels for Rayleigh-wave phase velocities at 100 s period and for Rayleigh-wave group velocities at 20 s period.

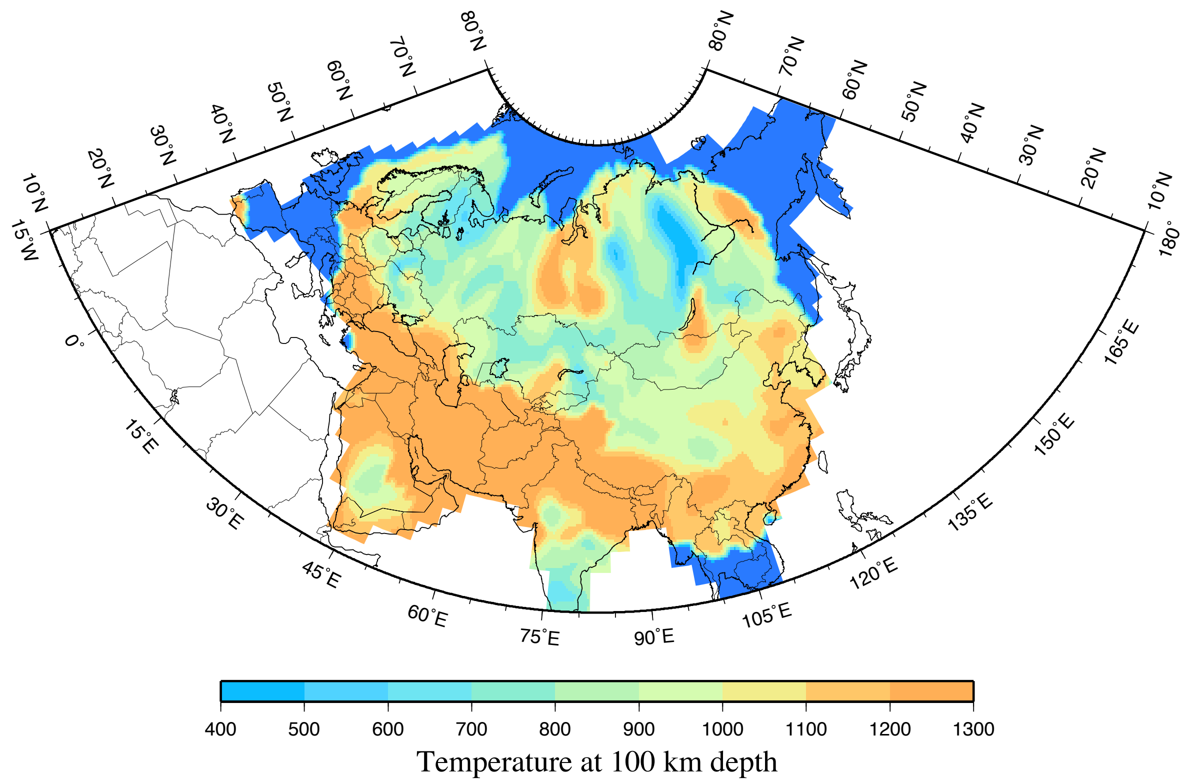


Figure 12: Map of estimated mantle temperatures at a depth of 100 km for Eurasia (adapted from *Artemieva and Mooney* [2001]).

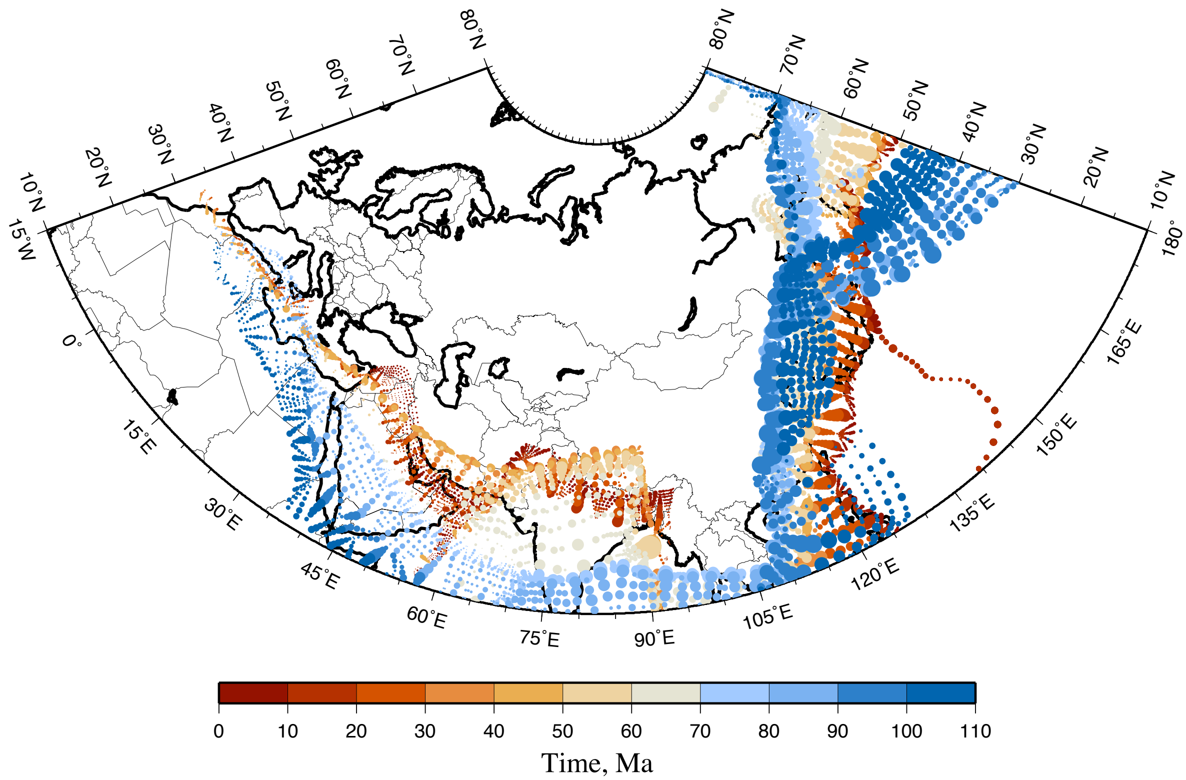


Figure 13: Map of subduction at a depth of 300 km during the past 110 My. Areas of the circles are proportional to the volume of subducted material. Values are those compiled by *Steinberger and O'Connell* (1998) using data from *Gordon and Jurdy* (1986) for the period between 0 and 64 Ma and from *Lithgow-Bertelloni* (1994) for earlier years.

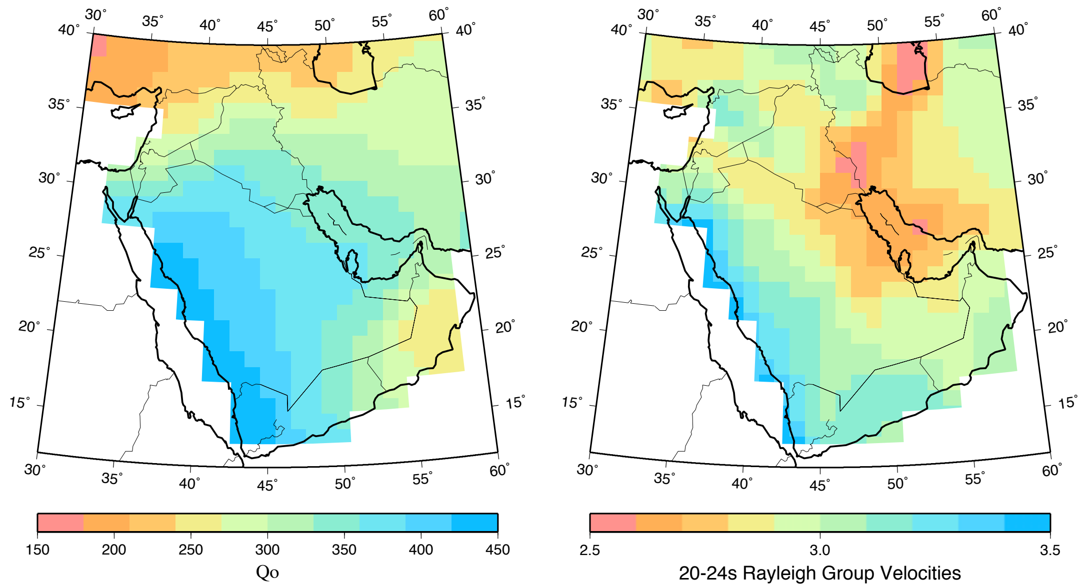


Figure 14: Left - $Q_{Lg}^{C}$ for 1-Hz $Lg$ coda ($Q_o$) (adapted from *Cong and Mitchell* [1998]), and Right - 20-s Rayleigh-wave group velocities for the Arabian Peninsula (adapted from *Mokhtar et al.* [2001]).

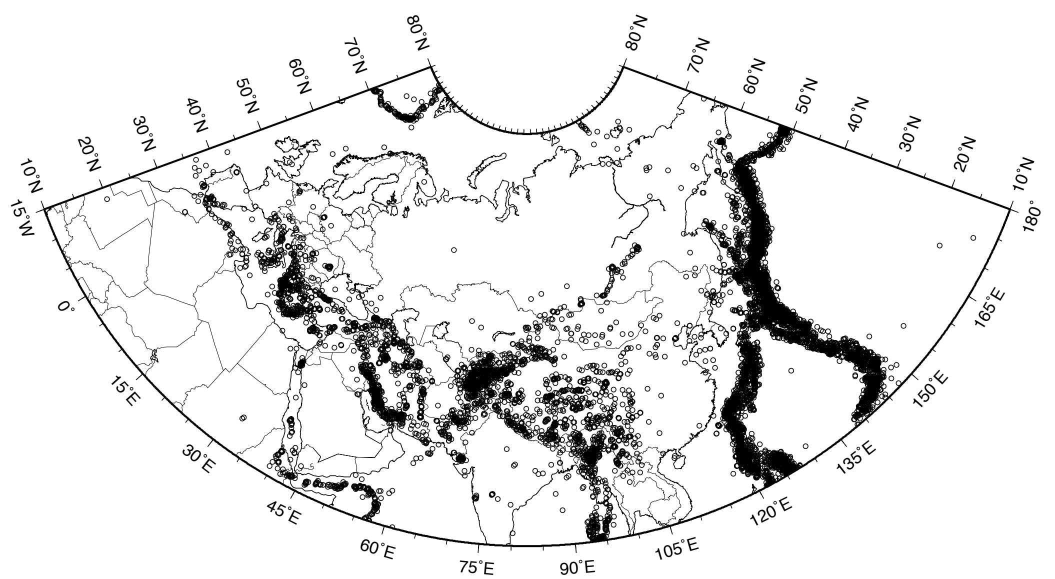


Figure 15: Map of earthquake epicenters for events of magnitude greater than 4.5 that occurred between 1995 and 2001.

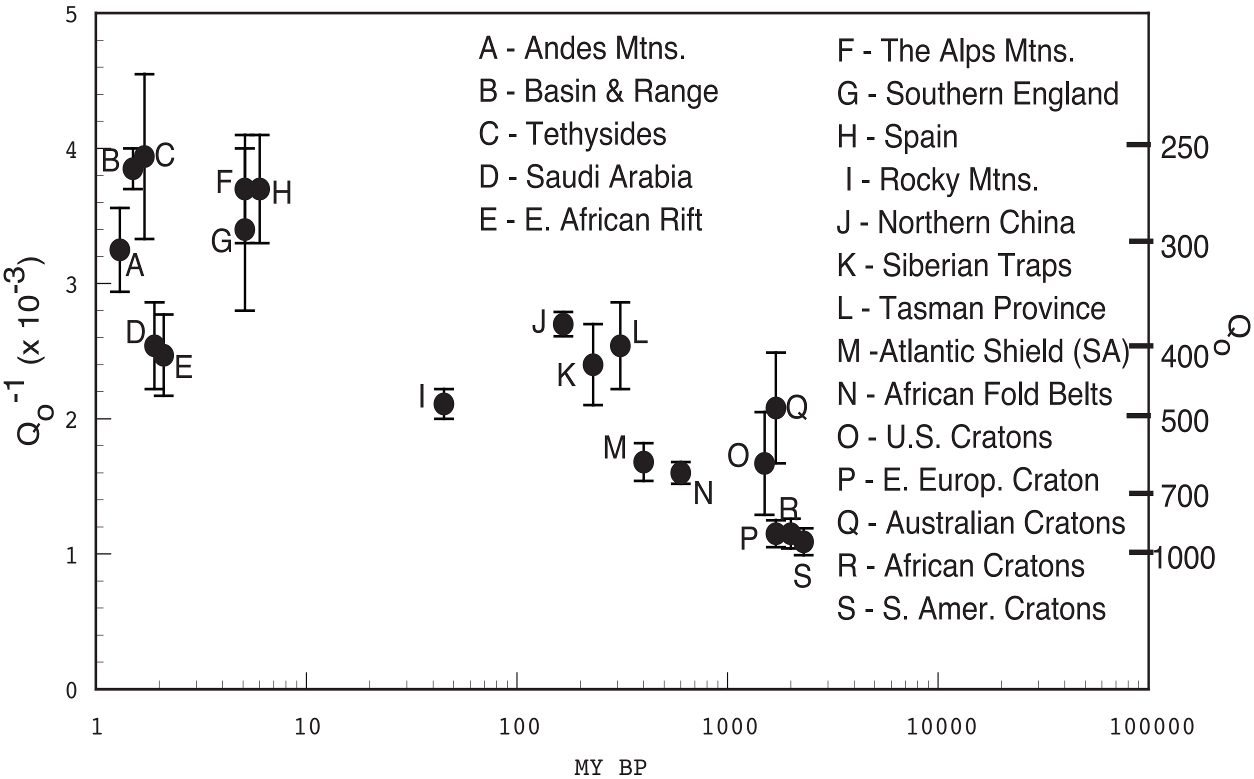


Figure 16: Variation of $Q_o$ with time since the most recent episode of major tectonic or orogenic activity in selected regions where it has been well determined.

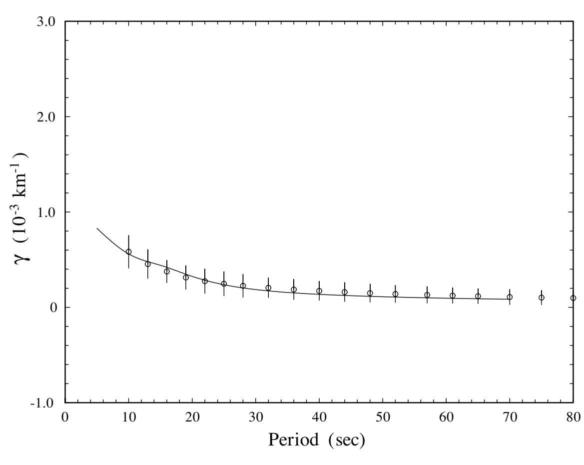


Figure 17: Example comparison of $\gamma_R$ curves obtained using $Q_o$ and $\eta$ values from Figures 5 and 6 and the empirically derived factor for $\eta$ (solid line) with measured $\gamma_R$ curves (symbols). The measured values (symbols) are averages determined using recordings at nearby station pairs YSS-HIA and YSS-MDJ for an event in central China.

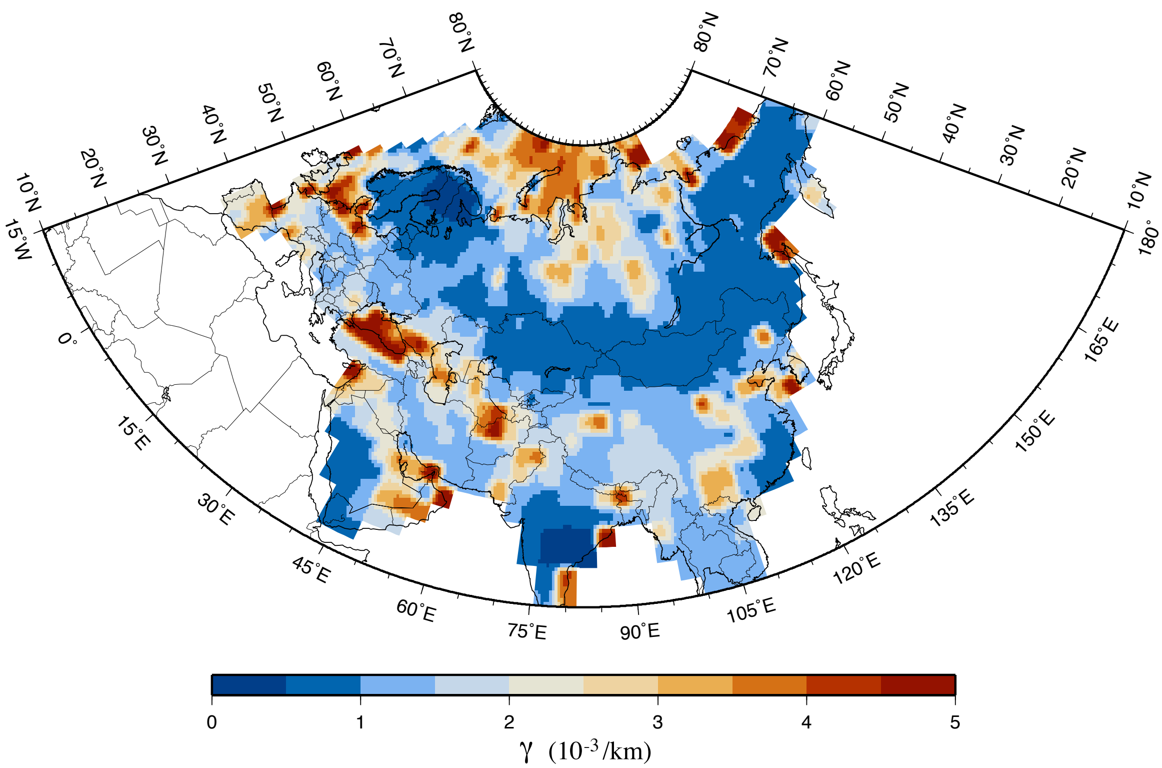


Figure 18: Rayleigh-wave attenuation coefficients at a period of 5 s obtained from $Q_o$ and $\eta$ values in Figures 5 and 6 assuming that $Q_\alpha = 2Q_\mu$.

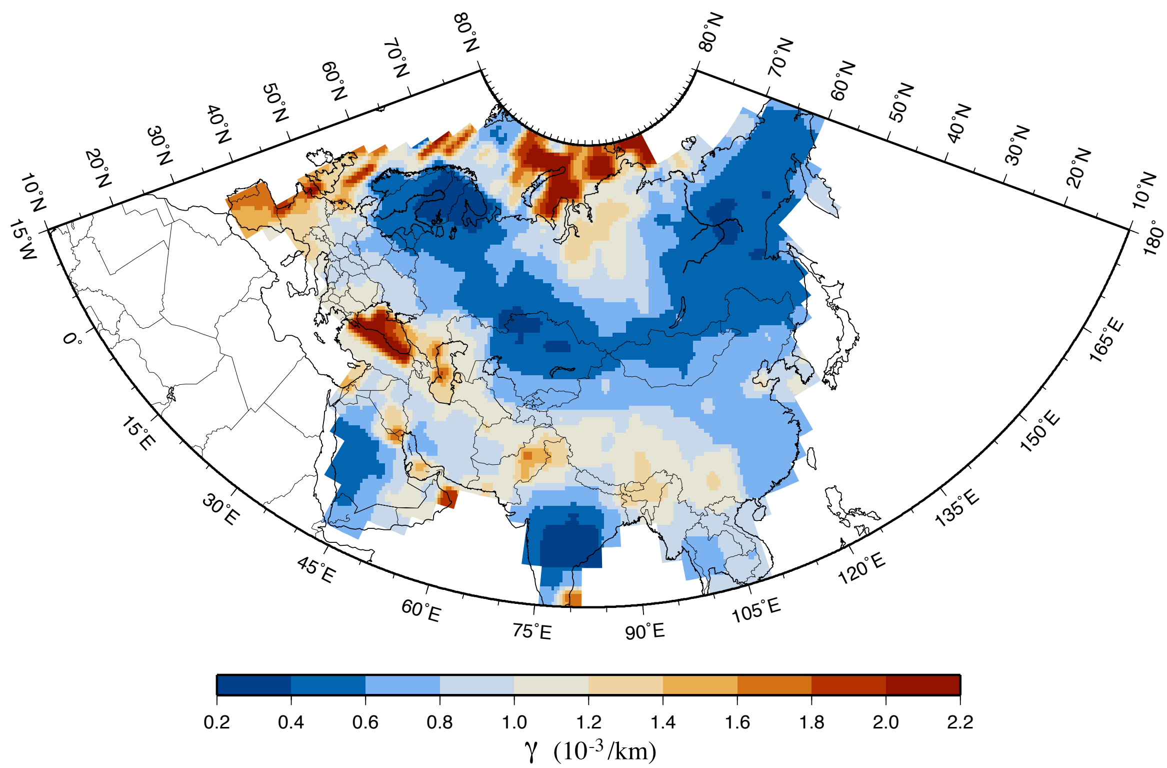


Figure 19: Rayleigh-wave attenuation coefficients at a period of 10 s obtained from $Q_o$ and $\eta$ values in Figures 5 and 6 assuming that $Q_\alpha = 2Q_\mu$.

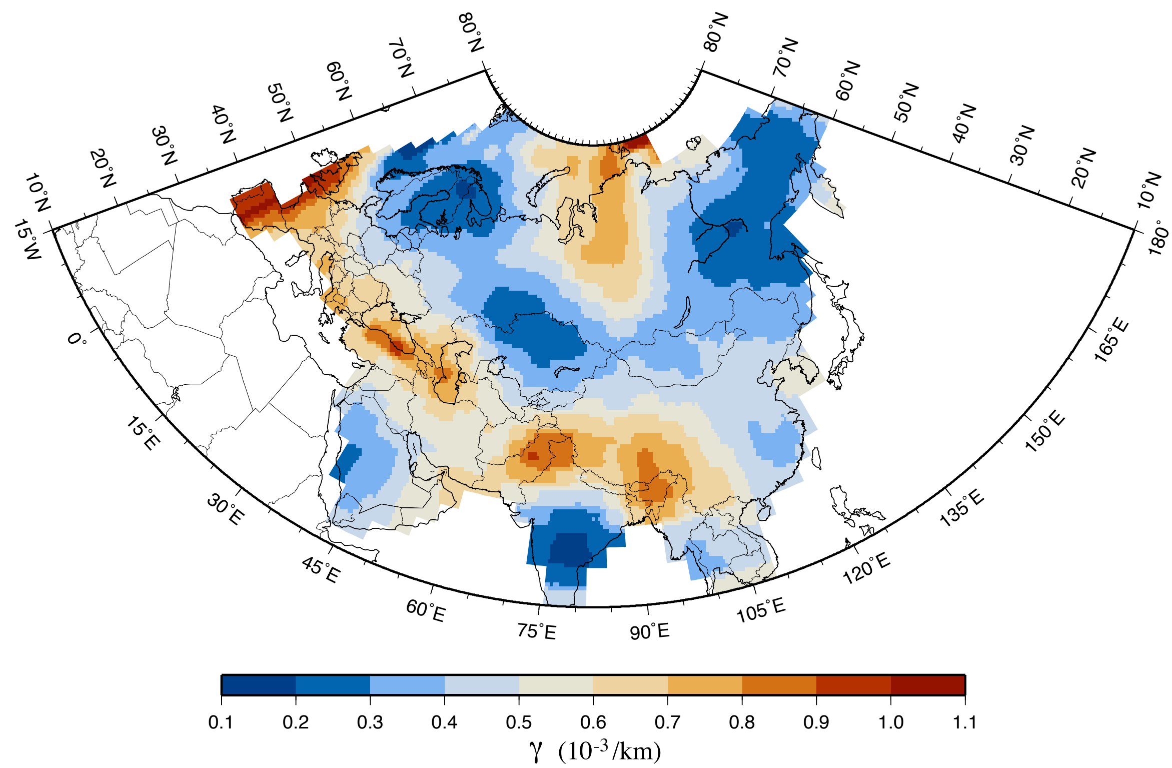


Figure 20: Rayleigh-wave attenuation coefficients at a period of 20 s obtained from $Q_o$ and $\eta$ values in Figures 5 and 6 assuming that $Q_\alpha = 2Q_\mu$.

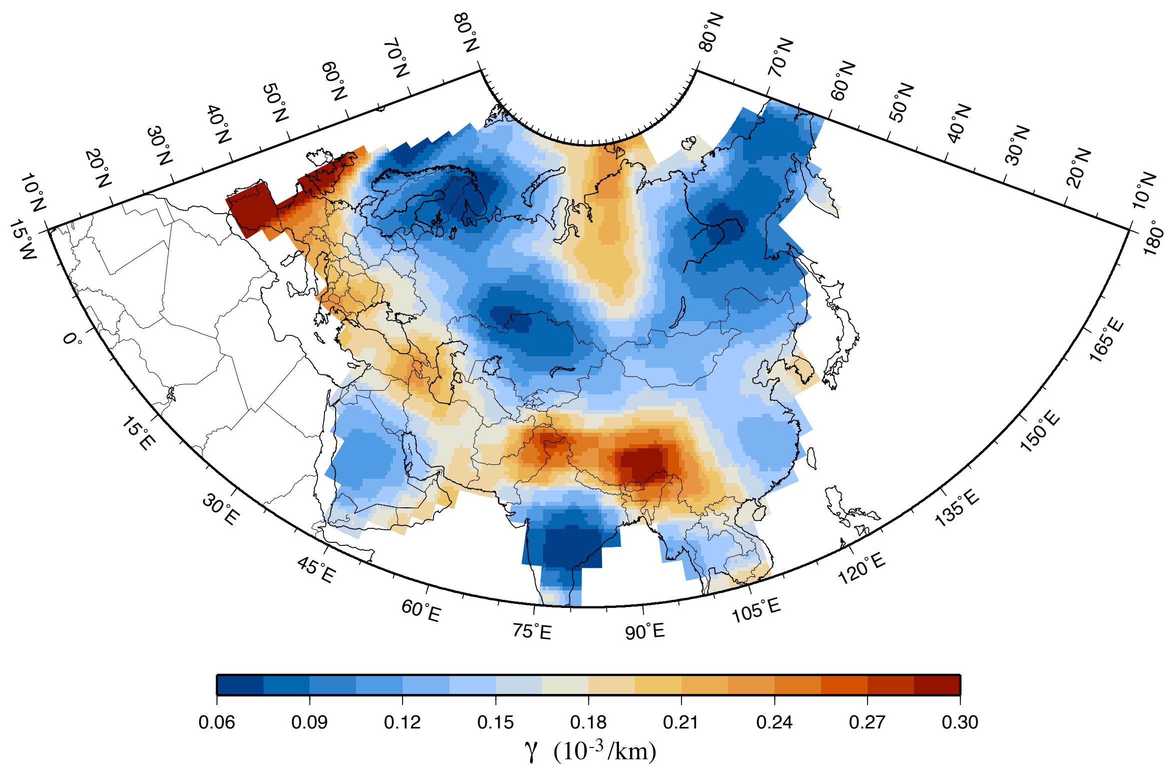


Figure 21: Rayleigh-wave attenuation coefficients at a period of 50 s obtained from $Q_o$ and $\eta$ values in Figures 5 and 6 assuming that $Q_\alpha = 2Q_\mu$.

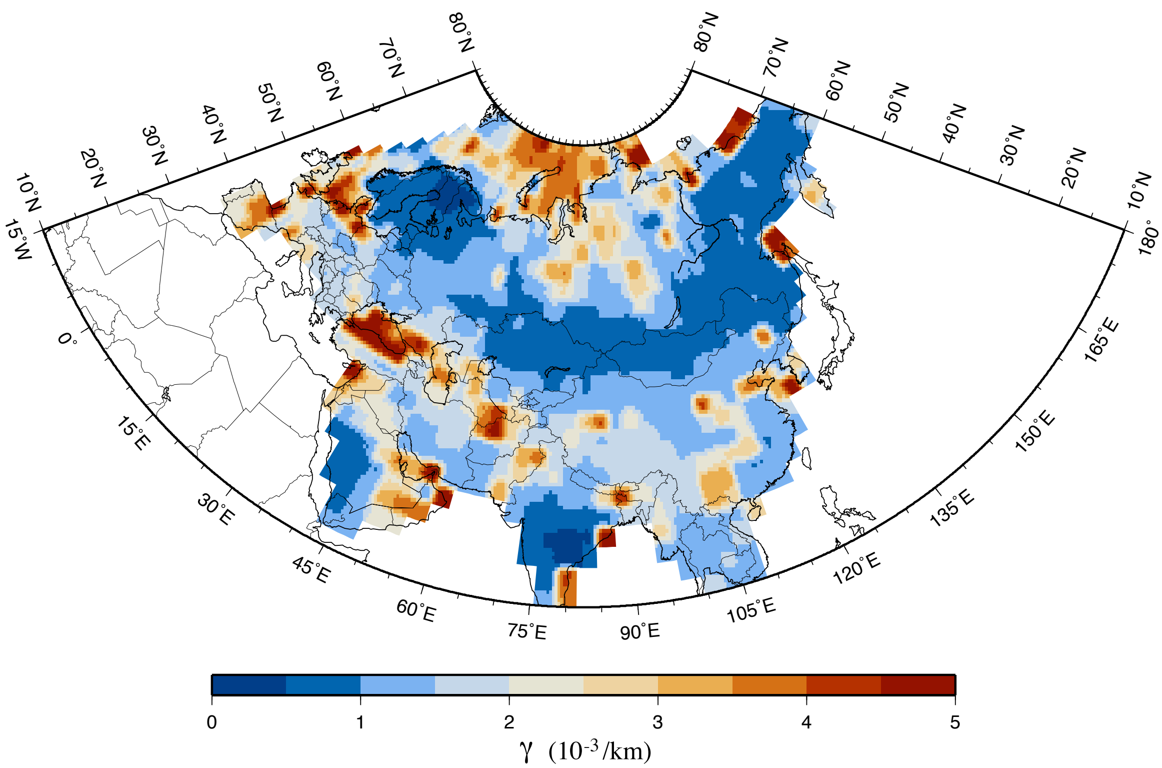


Figure 22: Rayleigh-wave attenuation coefficients at a period of 5 s obtained from $Q_o$ and $\eta$ values in Figures 5 and 6 assuming that $Q_\alpha = Q_\mu$.

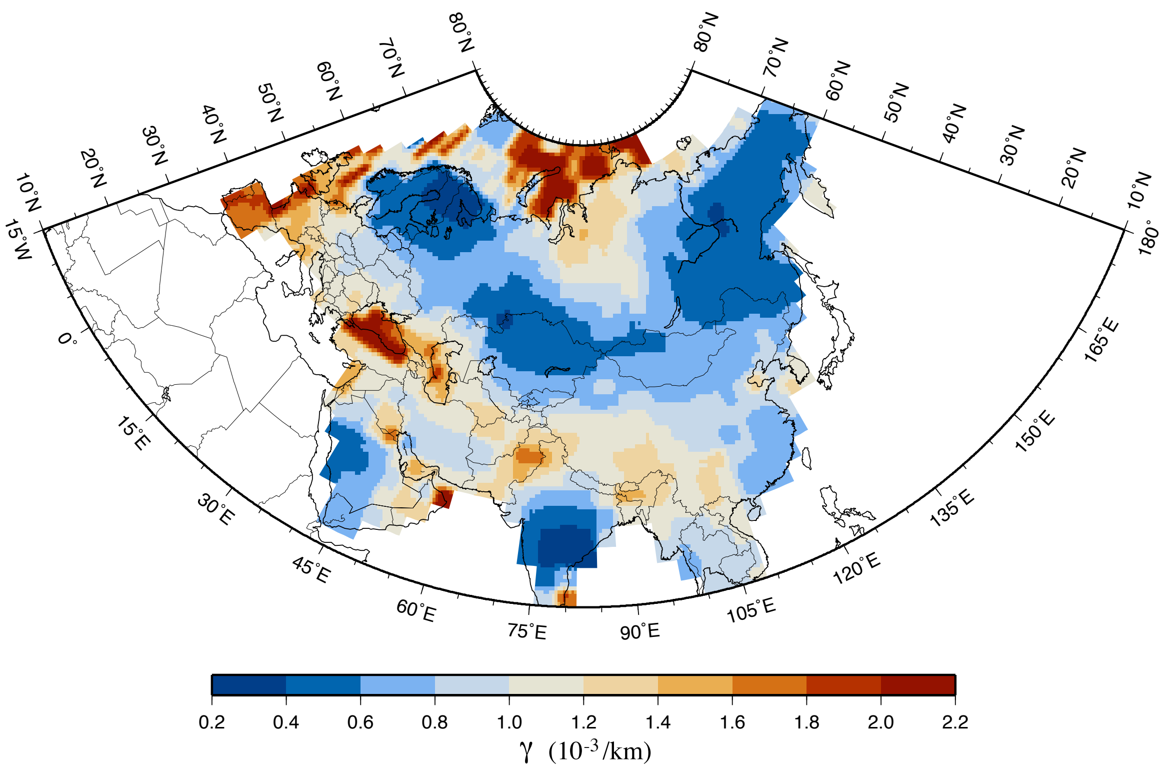


Figure 23: Rayleigh-wave attenuation coefficients at a period of 10 s obtained from $Q_o$ and $\eta$ values in Figures 5 and 6 assuming that $Q_\alpha = Q_\mu$.

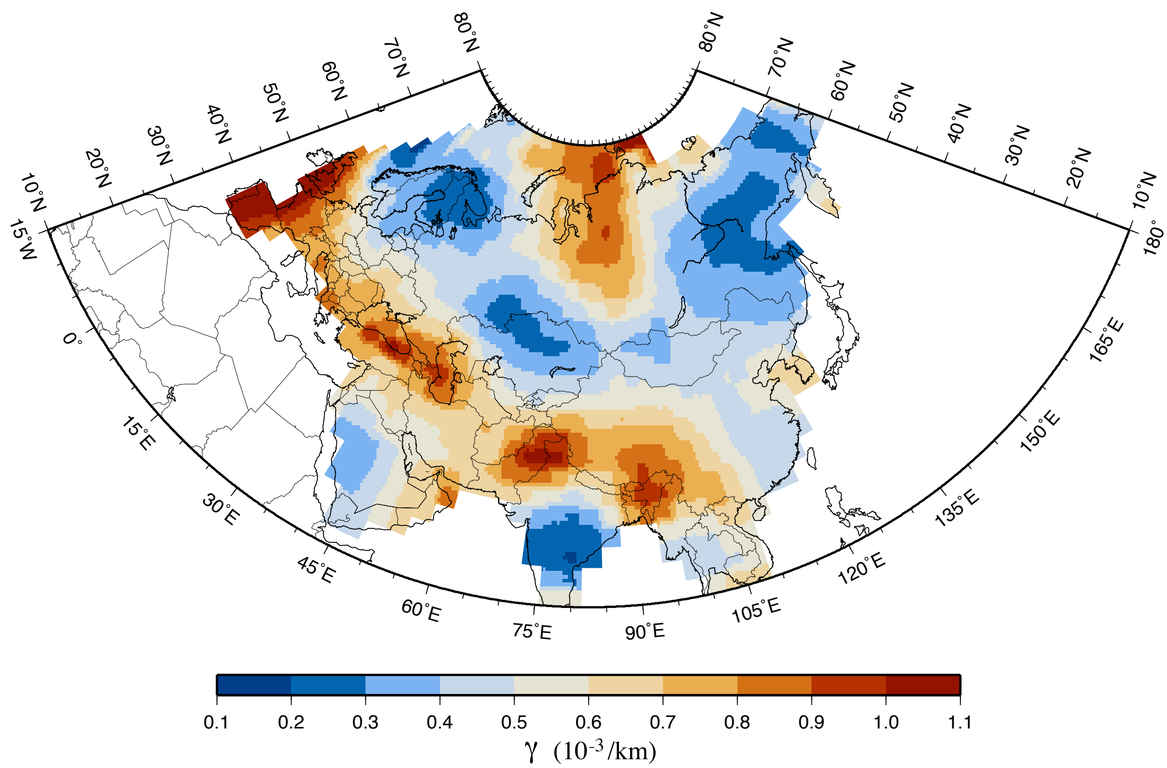


Figure 24: Rayleigh-wave attenuation coefficients at a period of 20 s obtained from $Q_o$ and $\eta$ values in Figures 5 and 6 assuming that $Q_\alpha = Q_\mu$.

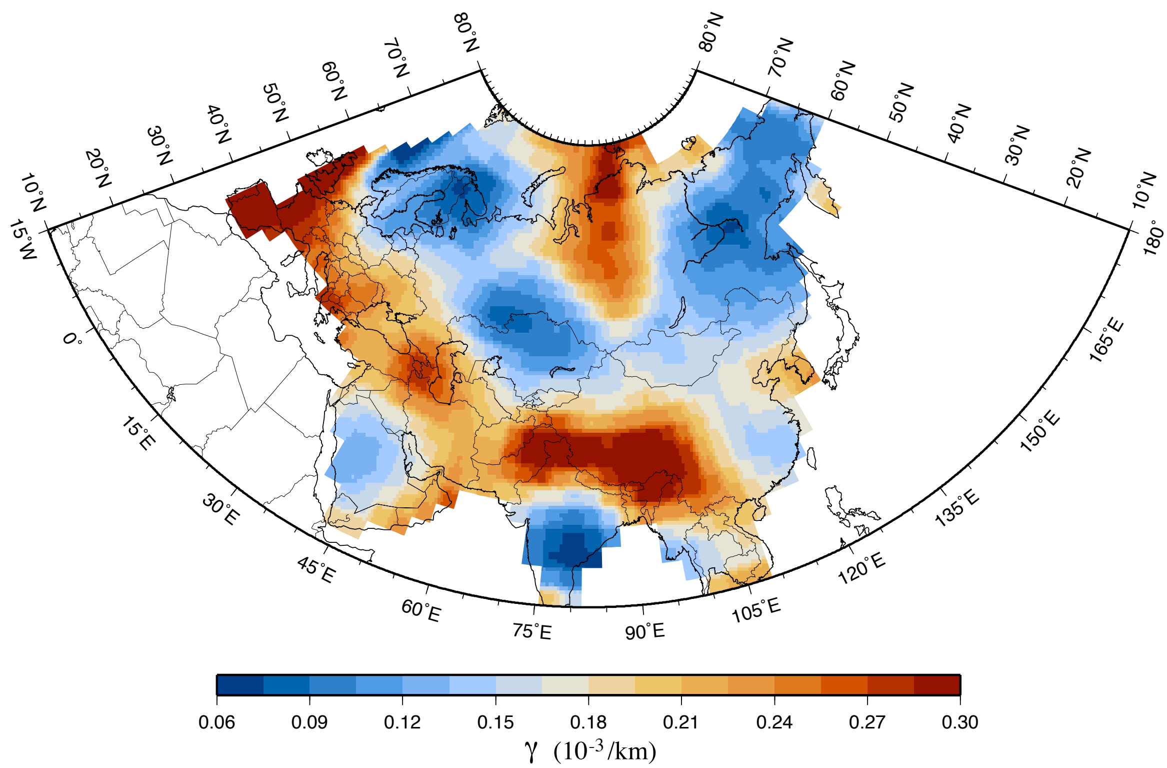


Figure 25: Rayleigh-wave attenuation coefficients at a period of 50 s obtained from $Q_o$ and $\eta$ values in Figures 5 and 6 assuming that $Q_\alpha = Q_\mu$.